J. Fluid Mech. (2002), *vol.* 450, *pp.* 169–199.
DOI: 10.1017/S0022112001006383 Printed in the United Kingdom

Start-up flows in a three-dimensional rectangular driven cavity of aspect ratio 1:1:2 at $Re = 1000$

By J.-L. GUERMOND[1], C. MIGEON[2], G. PINEAU[3] AND L. QUARTAPELLE[4]

[1]Laboratoire d'Informatique pour la Mécanique et les Sciences de l'Ingénieur, CNRS, BP 133, 91403, Orsay, France
guermond@limsi.fr

[2]Laboratoire de Mécanique Appliquée, Automatique et Géomécanique, Institut National des Sciences Appliquées, 20 avenue des Buttes de Cèsmes – CS 14315, 35043 Rennes cedex, France
christophe.migeon@inh.fr

[3]Laboratoire d'Etudes Aérodynamiques (LEA), Université de Poitiers, CNRS, Boulevard Marie et Pierre Curie Téléport 2, BP 179, 86960 Futuroscope cedex, France

[4]Dipartimento di Ingegneria Aerospaziale, Politecnico di Milano, Via La Masa 34, 20158 Milano, Italy

(Received 26 May 2000 and in revised form 1 June 2001)

This paper provides comparisons between experimental data and numerical results for impulsively started flows in a three-dimensional rectangular lid-driven cavity of aspect ratio 1:1:2 at Reynolds number 1000. The initial evolution of this flow is studied up to the dimensionless time $t = 12$ and is found both experimentally and numerically to exhibit high sensitivity to geometrical perturbations. Three different flow developments generated by very small changes in the boundary geometry are found in the experiments and are reproduced by the numerics. This indicates that even at moderate Reynolds numbers the predictability of three-dimensional incompressible viscous flows in bounded regions requires controlling the shape of the boundary and the values of the boundary conditions more carefully than needed in two dimensions.

1. Introduction

1.1. *Lid-driven cavity flow: from two- to three-dimensional*

The study of viscous recirculating flows in bounded domains constitutes an important branch of fundamental fluid mechanics. A recent review on the subject can be found in Shankar & Deshpande (2000). The interest in this type of flow started with the experiments of Mills (1965) and Pan & Acrivos (1967) who provided visualizations of the flow in three-dimensional rectangular cavities of different aspect ratios, and with the work of Kawaguti (1961) and Burggraf (1966) who computed the steady two-dimensional flow driven by a moving wall in a square cavity. Steady solutions of the two-dimensional lid-driven-cavity (LDC) problem have been extensively computed with a variety of numerical methods using either the vorticity and stream function equations (Ghia, Ghia & Shin 1982), or the biharmonic formulation (Schreiber & Keller 1983 and Barragy & Carey 1997), or the primitive variable representation (Botella & Peyret 1998). For the square configuration and for Reynolds numbers in the range $1500 \leqslant Re \leqslant 10\,000$, it is established that there exist stable solutions consisting of a large primary eddy and three secondary eddies located near the

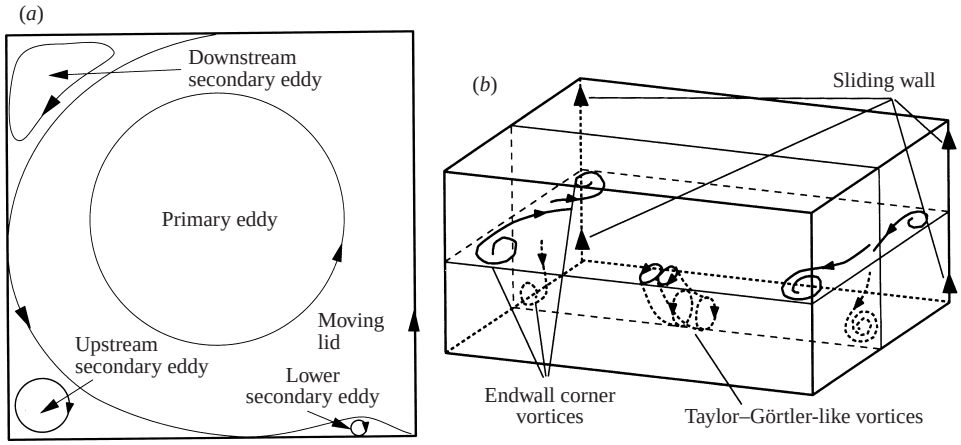

FIGURE 1. (*a*) Typical steady-flow patterns in the two-dimensional square cavity and (*b*) schematic of some flow structures in a three-dimensional rectangular cavity.

cavity corners, hereafter referred to as downstream secondary eddy (DSE), upstream secondary eddy (USE) and lower secondary eddy. Figure 1(*a*) gives a schematic picture of the basic steady-flow structure.

Time-dependent solutions of the two-dimensional lid-driven cavity problem for moderate to high Reynolds numbers were computed by Gustafson & Halasi (1986) using a projection method. These authors investigated the formation and the evolution of vortices together with the existence of periodic solutions. One critical aspect of the simulation of fluid motion in rectangular regions is the singularity of the problem in the two corners where the moving lid is in contact with the fixed walls. This has led investigators to regularize the velocity boundary condition. The regularization introduces an arbitrariness in the definition of the problem however and has not yet permitted a precise determination of the value of the critical Reynolds number for transition to unsteadiness for the two-dimensional flow in a square domain, the most recent estimate being $Re_c \approx 8000$ by Fortin *et al.* (1997). As will be shown in the present paper, the singularity of the lid-driven cavity combined with the three-dimensionality of the flow can have substantial effects on the development of the fluid motion in the three-dimensional rectangular cavity.

The two-dimensional model gives only a first approximation since in experiments the cavity is limited in span by endwalls, with important three-dimensional effects induced by the no-slip conditions imposed thereon. Experimental measurements and visualizations in cross-section confirm the overall qualitative agreement with two-dimensional solutions, but quantitative comparisons of secondary eddy sizes and velocity profiles fail, for the secondary eddies are smaller in experiments than in the two-dimensional model, with the velocities reduced in the three-dimensional configuration with respect to the two-dimensional one. These differences are a consequence of the spanwise component of the fluid motion.

Insightful experimental work was undertaken by Koseff & Street (1982, 1984*a*, *b*, *c*) and Rhee, Koseff & Street (1984) to depict the three-dimensional structure of LDC flows in cavities of square cross-section, various length-to-width aspect ratios, and for different Reynolds numbers based on the cross-section width. The three-dimensional structure of lid-driven cavity flows was first demonstrated numerically by de Vahl Davis & Mallison (1976) for the 1:1:3 cavity at $Re = 100$. The study of spanwise fluid

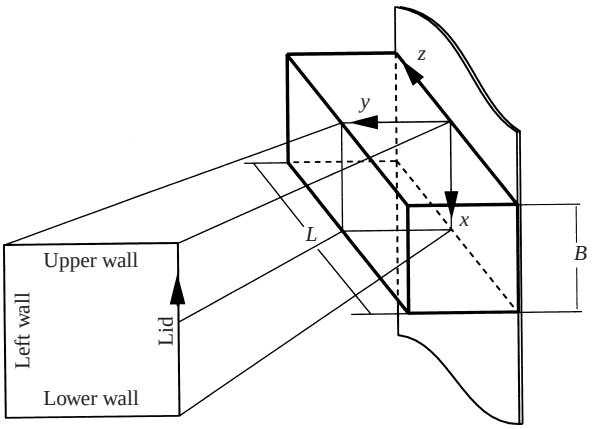

FIGURE 2. Boundary nomenclature and reference frame.

transport was subsequently extended to larger Reynolds numbers and other aspect ratios of the cavity by Freitas *et al.* (1985) and Freitas & Street(1988). Figure 1 depicts typical views of the steady flow in planes perpendicular to the lid-plane (*a*) and inside the cavity (*b*). Spanwise views reveal the presence of secondary flows corresponding to local and global vortices (see also Prasad & Koseff 1989):

(i) The local eddies are located in the region close to the corners and near the end-extremities of the cavity and are associated with fluid transport in the spanwise direction. The detailed numerical investigation of Chiang, Sheu & Hwang (1998) revealed the major role played by the end vortices in the spanwise transport.

(ii) The global eddies are regularly distributed along the cavity span in planes perpendicular to the lid and stretch along the streamlines of the primary recirculating flow. They are usually referred to as Taylor–Görtler-like (TGL) vortices, for they are much like the Taylor vortices occurring between rotating cylinders and the Görtler vortices occurring in the boundary layer over a concave surface. The TGL vortices occur in counter-rotating pairs, and are created in the DSE region of the cavity.

The success of numerical techniques to simulate accurately two-dimensional flows in enclosures for Reynolds numbers up to 10 000 and beyond encouraged researchers to tackle the three-dimensional problem directly at the relatively high Reynolds number $Re = 3200$. For instance, the solution of the three-dimensional cavity of aspect ratio 1:1:3 up to the dimensionless time $t \approx 190$ was computed by Freitas *et al.* (1985). The first comparisons between experiments and calculations gave only a qualitative agreement however. The difficulty in obtaining accurate solutions was confirmed in a 1991 GAMM workshop that was devoted to this problem, see Deville, Le & Morchoisne (1992). Even though the velocity fields in the symmetry plane at times $t = 50, 100, 200$ were predicted consistently by most participants, quite different flow patterns in spanwise cross-sections were obtained. These disagreements are due to the complexity of the three-dimensional dynamics which leads to difficulty in reproducing accurately fine spatial and temporal features at a discrete level. We have encountered similar difficulties in preliminary computations of the unsteady solution to this problem. While a good agreement with the other computed solutions referred to above was obtained for the velocity profiles in the symmetry plane of the cavity, a quantitative comparison of the number and position of the Taylor–Görtler vortices in spanwise sections was almost impossible. Thus, we found that the computation of deterministic solutions to the three-dimensional cavity problem at $Re = 3200$ for

$t \geqslant 100$ is very difficult. The situation on the experimental side was even worse. With the aid of the apparatus and under the conditions to be described in the following, we found it impossible to obtain reproducible visualizations at this relatively high Reynolds number for times as small as $t \approx 10$. We came to the conclusion that quantitative comparisons between experiments and calculations are feasible only by reducing the Reynolds number, and/or the time range, and/or the aspect ratio of the cavity. Since our initial goal was to make detailed comparisons on time-dependent three-dimensional laminar incompressible viscous flows, we decided to restrict our attention to the study of the driven cavity of aspect ratio 1:1:2 at the Reynolds number $Re = 1000$; see figure 2 for the cavity dimensions and the definition of the reference frame.

1.2. *Aim of the study*

The objectives of the paper are threefold:

The first goal is to investigate the progressive development of the three-dimensional flow in a rectangular cavity at $Re = 1000$ for $t = 0$ up to $t = 12$. Since the pioneering work of Koseff & Street (1982, 1984*a*, *b*, *c*), the start-up phase of this flow has not been investigated experimentally, to the best of our knowledge. We present detailed experimental and numerical descriptions of the evolution of the primary and secondary eddies during this phase.

Second, we describe the great sensitivity of this flow to perturbations on the boundary conditions. In particular, we study the way in which tiny modifications of the upper-wall surface triggers the growth of Taylor-type vortices. Two perturbed configurations are considered in the present work and the corresponding flows are compared to the unperturbed flow. The tiny geometrical modifications consist in localized protuberances on the upper-wall near the right corner, as described in detail in § 5.2. To underline the critical role played by these wall perturbations, we show in figure 3 the experimental and numerical spanwise velocity fields in plane $y = \frac{1}{2}$ at time $t = 12$ of the unperturbed flow and of the corresponding flow that is observed when three tiny perturbations are present. The figure shows that each perturbation induces one vortex pair (due to the flow symmetry, only half of the cavity is represented in each plot). This introductory picture shows that, when performing experiments, great attention must be paid to avoiding wall perturbations (e.g. air bubbles, scratches, etc.) close to the intersection of the lid with the fixed walls in order to prevent the birth of additional instabilities.

The third goal is to show the present-day capability in performing accurate comparisons between experiments and computations for three-dimensional unsteady flows in bounded regions, at least under the restrictions mentioned above. In this respect, the second-order finite element projection that was developed by Guermond & Quartapelle (1997), briefly described in § 3, is found to be a reliable and accurate predictive tool.

2. Experimental apparatus

In this section we present the experimental apparatus and the visualization techniques that we used to perform our experiments.

2.1. *Method*

Experiments were carried out in a modified version of an apparatus designed to study laminar flows of incompressible viscous fluids downstream of impulsively started ob-

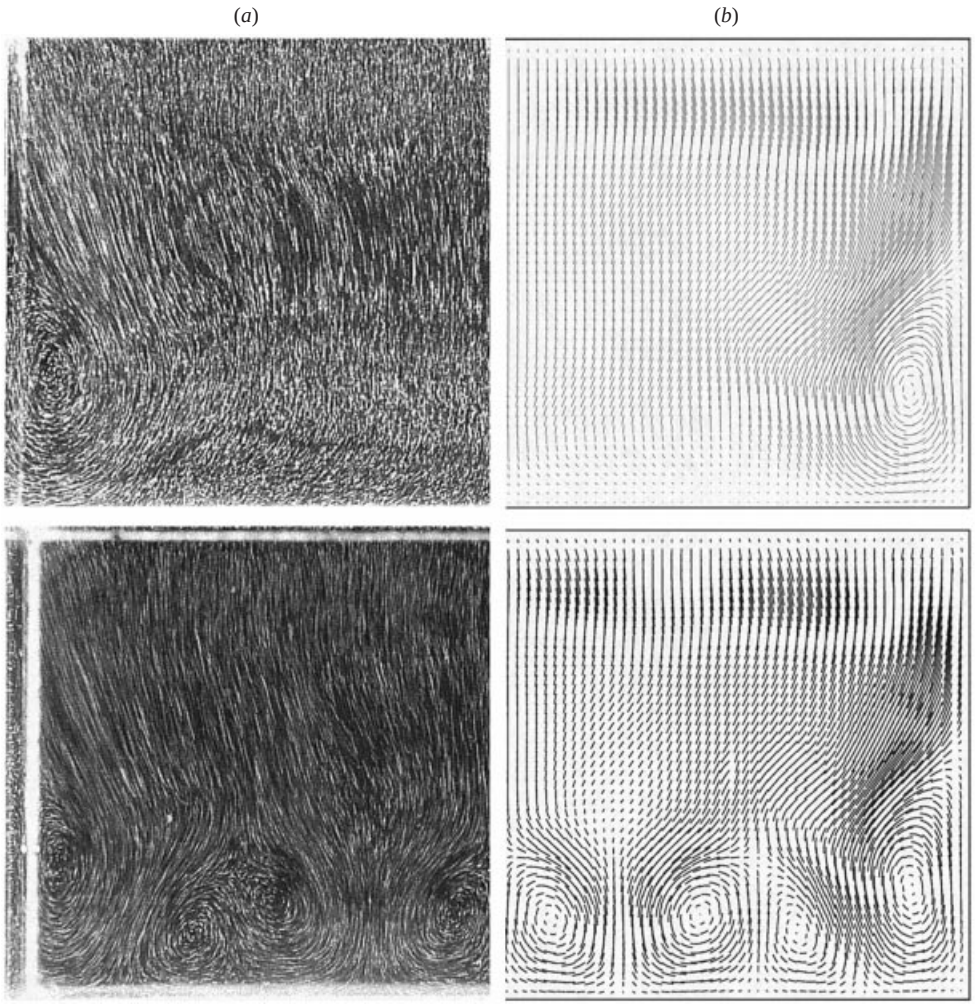

FIGURE 3. Comparisons of the flow observed in the smooth cavity (top) with the flow observed in the cavity perturbed with three tin ribbons (bottom) at $t = 12$ in plane $y = \frac{1}{2}$: (*a*) experiments; (*b*) computations. Due to symmetry of the flow, only half of the cavity is shown in each plot.

stacles. A detailed description of the equipment is provided by Boisaubert, Coutanceau & Ehrman (1996). Here we give only a brief description of its adaptation to cavity flows by Migeon, Texier & Pineau (1998, 2000). A diagram of the experimental arrangement is given in figure 4.

In previous experimental work, the fluid motion inside the cavity was induced by a rotating cylinder (Pan & Acrivos 1967) or a moving belt (Koseff & Street 1982, 1984*a*, *b*, *c*) placed at the top of a fixed cavity. In the present equipment, the cavity slides smoothly downward along a fixed large vertical plate acting as a lid. Flow development is sequentially recorded by a computer-controlled camera which follows the cavity in its motion so that, in the camera frame, the cavity is fixed and the plate is the moving lid. The cavity is towed inside a vertical water tank with a capacity of $80 \times 100 \times 120\,\mathrm{cm}^3$, and is attached to the towing frame by means of metal rods which maintain it horizontal and guide its fall. Spring-leaves, located at the cavity end-extremities, maintain continuous contact between the lid and the cavity to avoid leak-

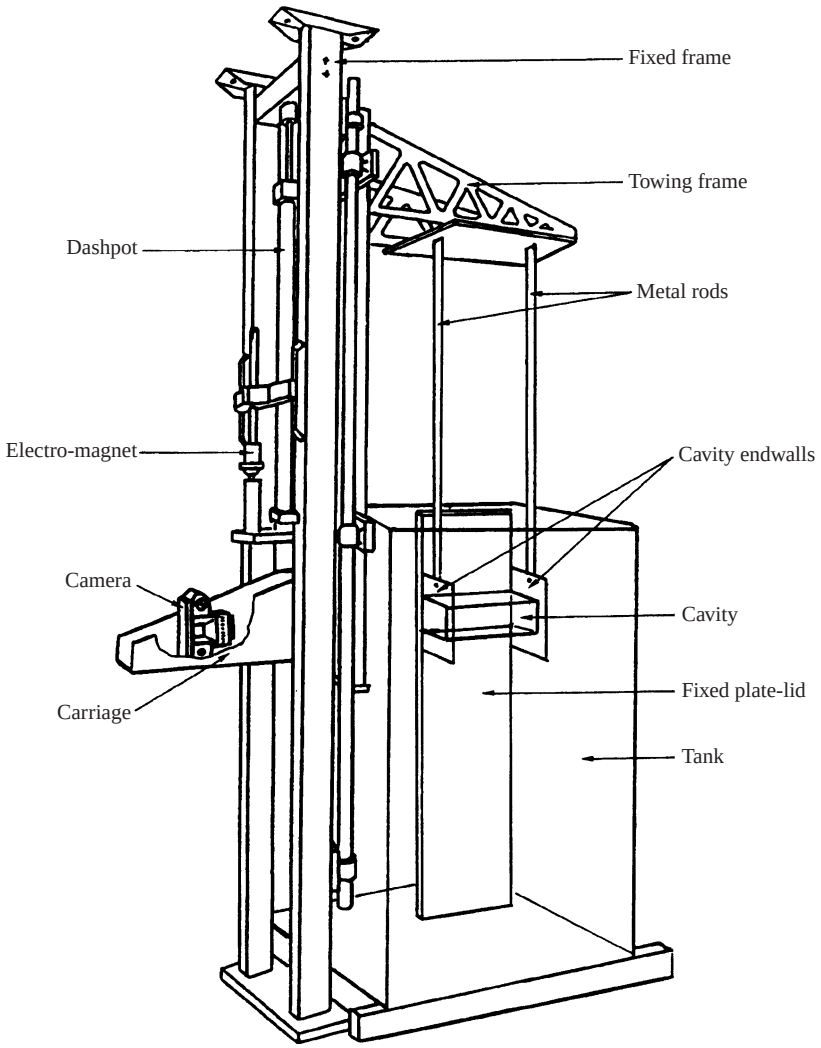

FIGURE 4. Experimental set-up.

age. Experiments were performed with a square-section cylindrical cavity of width $B = 6.2\,\text{cm}$ and length $L = 12.4\,\text{cm}$. Notation and reference frame are shown in figure 2.

To allow visualizations, the tank and the cavity walls are made of altuglass and both are filled with water. Before every experiment, the cavity carriage is attached to a fixed electromagnet and left until the fluid comes to rest. At the initial time, the carriage is released. The mobile carriage acceleration phase is about 0.05 s, which corresponds to 1.46% of a dimensionless time unit. After this short initial period, a constant downward velocity U is ensured under the combined action of gravity and a damping dashpot.

In this study, the cavity velocity, i.e. the relative velocity of the lid, is $U = 1.8\,\text{cm}\,\text{s}^{-1}$, defining the Reynolds number $Re = UB/\nu = 1000$ where ν is the kinematic viscosity of water. Using B/U as the reference time scale, the time interval that we study is $0 \leqslant t \leqslant 12$, the upper limit being imposed by the vertical extent of the tank. A picture is recorded each time the lid has travelled a distance equal to the cavity width B.

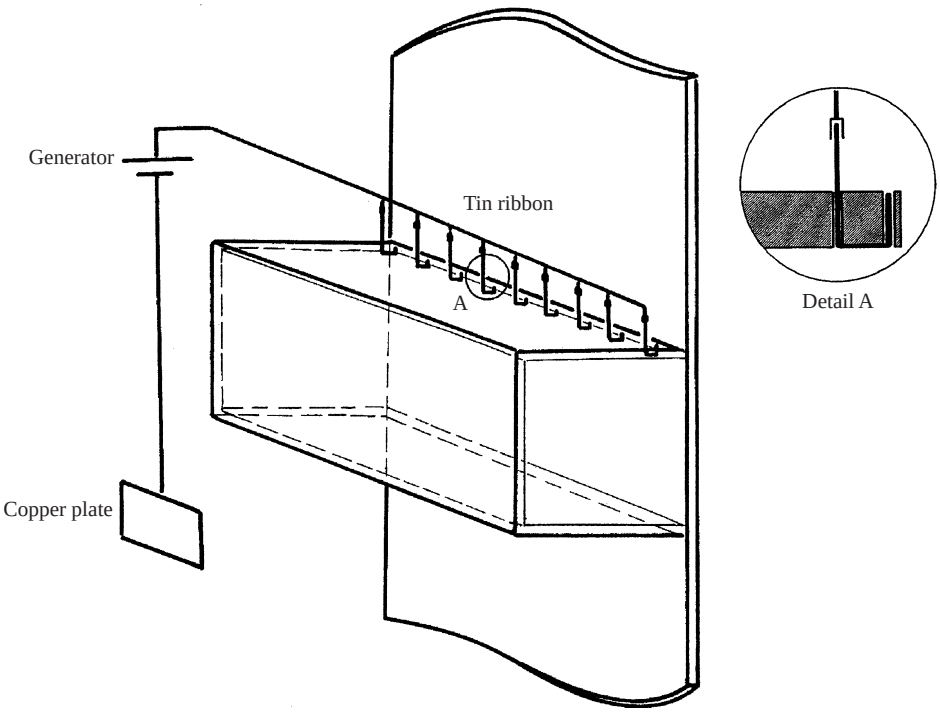

FIGURE 5. Principle of the continuous dye-emission technique.

2.2. *Visualization techniques*

To analyse the flow development, two complementary visualization techniques coupled with a laser sheet illumination have been used: one based on continuous dye emission and the other using particle streaks.

For the dye-emission technique, emission lines are generated by the electrolysis of tin ribbons (5 mm long). The tin ribbons are set in grooves tooled in the upper wall of the cavity as illustrated by detail A in figure 5. A DC tension of the order of 20 V is applied between the tin wires (anode) and a copper sheet (cathode) immersed in the tank. When the flow develops, tin salt released from the ribbons is shed in the form of rolling-up filaments (see § 4.1). Note that in the dye-emission technique the fluid particles dyed by electrolysis have zero initial velocity, as opposed to non-zero initial velocity occurring in dye-injection techniques. Thus the dye technique adopted here does not perturb the delicate nature of the flow's start-up phase.

In some experiments, nine dye-emission points are placed uniformly along the cavity span as depicted in figure 5. In other experiments three or only one dye-emission points are used (as shown in figure 3 and later).

For the particle-streak technique, tiny particles are uniformly dispersed in the cavity volume. These particles are spherical, of average diameter $\approx 10\,\mu$m, made of silvered glass, and of neutral buoyancy. When the fluid is set in motion, the solid particles follow the trajectory of the flow. During the exposure time, the paths of the lit particles give an instantaneous picture of the flow (see § 4.1). After analysis, these pictures yield information on the flow topology (dimensions and positions of eddies) and the flow kinematics (velocities). The velocity field is then deduced by meticulous measurements of the streak lengths on enlarged negatives. The relative accuracy of

all measurements is found to be better than 3%. To capture the details of the onset of the flow three-dimensionality, visualizations have been made in transverse cross-sections (parallel to the x, y-plane) and in spanwise cross-sections (parallel to the x, z- or y, z-planes).

For a given plane, experiments have been repeated at least four times for reliability.

3. Numerical method

In this section we briefly describe the numerical method that we used to solve the time-dependent Navier–Stokes equations.

3.1. *Navier–Stokes equations*

The equations governing incompressible viscous flows are expressed here in terms of the primitive variables: velocity $\boldsymbol{u}$ and pressure p (per unit density). The mathematical statement of the problem is: find $\boldsymbol{u}$ and p (up to a constant) so that

$$\left.\begin{aligned} &\frac{\partial \boldsymbol{u}}{\partial t} - \nu\nabla^2\boldsymbol{u} + (\boldsymbol{u}\cdot\nabla)\boldsymbol{u} + \nabla p = 0, \\ &\nabla\cdot\boldsymbol{u} = 0, \\ &\boldsymbol{u}_{|\partial\Omega} = \boldsymbol{b}, \\ &\boldsymbol{u}_{|t=0} = \boldsymbol{u}_0, \end{aligned}\right\} \tag{3.1}$$

where ν is kinematic viscosity (assumed constant), $\boldsymbol{b}$ is the velocity prescribed on the boundary $\partial\Omega$ of the rectangular domain $\Omega = [0,1] \times [0,1] \times [-1,1]$, and $\boldsymbol{u}_0$ is the divergence-free initial velocity field.

In the reference frame defined in figure 2, the moving wall is the face $y = 0$, so that the velocity boundary condition is

$$\boldsymbol{b} = \begin{cases} -\hat{\boldsymbol{x}} & \text{if } y = 0 \\ 0 & \text{otherwise,} \end{cases} \tag{3.2}$$

where $\hat{\boldsymbol{x}}$ denotes the unit vector on the x-axis, which is parallel to the moving wall and vertical in the experimental setup. The initial condition assumes the fluid to be at rest.

3.2. *Incremental projection method*

The governing equations are solved by means of a fractional-step projection method using a spatial discretization based on mixed finite elements. This method is derived from the incremental version of the original projection method introduced by Chorin (1968, 1969) and Temam (1969). It consists in making explicit the pressure at the viscous step and correcting it at the projection step by evaluating a pressure increment to enforce the incompressibility condition. The incremental treatment of the pressure, also known as the 'pressure correction method', is a necessary prerequisite for developing discrete integration schemes with second-order time accuracy. In fact, the fractional-step structure of projection methods induces an irreducible time-splitting error of $O(\Delta t)$ for the nonincremental method and of $O((\Delta t)^2)$ for the incremental one, as shown by Guermond & Quartapelle (1997), Δt denoting the size of the time step.

A rigorous mathematical analysis of the incremental method has been provided by Guermond & Quartapelle (1998). Here, the complete set of equations to be solved is given without detailing their theoretical justification and derivation. First, the

incremental projection method with a first-order time discretization of the momentum equation is introduced to explain the basic elements of the strategy adopted for obtaining unconditional stability in time integration. Then, a second-order-accurate version of the method is described. The algorithm is based on a three-level backward difference formula (BDF) for the momentum equation.

The incremental projection method is defined as follows. Setting $\boldsymbol{u}^0 = \boldsymbol{u}_0$ and assuming p^0 to be known (in the present problem with the fluid at rest initially $p^0 \equiv 0$), for $k \geqslant 0$ solve the following two problems: first, consider the advection–diffusion step

$$\left.\begin{aligned} &\frac{\boldsymbol{u}^{k+1} - \boldsymbol{u}^k}{\Delta t} - \nu \nabla^2 \boldsymbol{u}^{k+1} + (\boldsymbol{u}^k \cdot \nabla)\boldsymbol{u}^{k+1} \\ &\qquad + \tfrac{1}{2}(\nabla \cdot \boldsymbol{u}^k)\boldsymbol{u}^{k+1} = -\nabla(2p^k - p^{k-1}), \\ &\boldsymbol{u}^{k+1}{}_{|\partial\Omega} = \boldsymbol{b}^{k+1}; \end{aligned}\right\} \tag{3.3}$$

then, perform the projection step in incremental (pressure correction) form expressed by the following Poisson equation for the pressure increment $(p^{k+1} - p^k)$:

$$\left.\begin{aligned} &-\nabla^2(p^{k+1} - p^k) = -(\Delta t)^{-1} \nabla \cdot \boldsymbol{u}^{k+1}, \\ &\frac{\partial(p^{k+1} - p^k)}{\partial n}{}_{|\partial\Omega} = 0. \end{aligned}\right\} \tag{3.4}$$

The time integration scheme chosen in the momentum equation is fully implicit for the viscous term and semi-implicit for the nonlinear advection term. To guarantee unconditional stability, i.e. to avoid any restriction on the time step Δt, the advection term $(\boldsymbol{u} \cdot \nabla)\boldsymbol{u}$ has been replaced by its well-known skew-symmetric counterpart $(\boldsymbol{u} \cdot \nabla)\boldsymbol{u} + \frac{1}{2}(\nabla \cdot \boldsymbol{u})\boldsymbol{u}$, see e.g. Temam (1977).

Note that the Neumann condition for the pressure in problem (3.4) is not a physical boundary condition, for no boundary condition is needed for pressure in incompressible flows. However, by virtue of the Ladyzhenskaya orthogonality theorem, also known as Hodge decomposition, underlying the projection method, the Neumann condition is the mathematically correct boundary condition for the Poisson pressure equation in the incremental projection method considered here.

Contrary to other projection algorithms, the end-of-step solenoidal velocity does not appear explicitly in (3.3)–(3.4), because it has been algebraically eliminated in favour of the intermediate one $\boldsymbol{u}^{k+1}$. This elimination is responsible for the appearance of the extrapolated pressure on the right-hand side of the viscous step. Note that the first time step ($k = 0$) does not require the elimination of the end-of-step velocity so that the right-hand side of the momentum equation in (3.3) for $k = 0$ has to be replaced by $-\nabla p^0$.

It has been demonstrated in Guermond & Quartapelle (1998) that $\boldsymbol{u}^{k+1}$ converges to the exact solenoidal velocity field in a stronger norm than the end-of-step velocity.

3.3. *Spatial discretization by a mixed finite element method*

Let $\mathscr{T}_h$ be a regular finite element mesh composed of tetrahedra. We define $\boldsymbol{X}_h$, the approximation space for the velocity, as the set of continuous functions that are piecewise quadratic on each tetrahedron of $\mathscr{T}_h$. The approximation space N_h for the pressure is composed of continuous functions that are piecewise linear on each tetrahedron. To ensure that the pressure is uniquely defined, we require it to have zero mean value.

The weak formulation of the advection–diffusion step (3.3) is: for $k \geqslant 0$, find $\boldsymbol{u}_h^{k+1} \in \boldsymbol{X}_h$ with $\boldsymbol{u}_h^{k+1}{}_{|\partial\Omega} = \boldsymbol{b}_h^{k+1}$, such that

$$\left(\frac{\boldsymbol{u}_h^{k+1} - \boldsymbol{u}_h^k}{\Delta t}, \boldsymbol{v}_h\right) + \nu \left(\nabla \boldsymbol{u}_h^{k+1}, \nabla \boldsymbol{v}_h\right) + \left((\boldsymbol{u}_h^k \cdot \nabla)\boldsymbol{u}_h^{k+1}, \boldsymbol{v}_h\right) + \tfrac{1}{2}(\nabla \cdot \boldsymbol{u}_h^k, \boldsymbol{u}_h^{k+1} \cdot \boldsymbol{v}_h) = -(\nabla(2p_h^k - p_h^{k-1}), \boldsymbol{v}_h), \tag{3.5}$$

for all $\boldsymbol{v}_h \in \boldsymbol{X}_h$ with $\boldsymbol{v}_{h|\partial\Omega} = 0$. The velocity $\boldsymbol{u}_h^1$ at the first time step is also evaluated from equation (3.5) with $k = 0$, with the right-hand side replaced by $-(\nabla p_h^0, \boldsymbol{v}_h)$, as already mentioned.

The weak form of the projection step takes the following form: for $k \geqslant 0$, find the pressure increment $(p_h^{k+1} - p_h^k) \in N_h$ such that

$$\left(\nabla(p_h^{k+1} - p_h^k), \nabla q_h\right) = -(\Delta t)^{-1} \left(\nabla \cdot \boldsymbol{u}_h^{k+1}, q_h\right), \tag{3.6}$$

for all $q_h \in N_h$. It is important to note that the use of polynomials of different order for velocity and pressure (here P_2 and P_1) guarantees the satisfaction of the *inf-sup* compatibility condition, also known as the Ladyzhenskaya–Babuška–Brezzi condition. This property prevents the occurrence of spurious modes on pressure. The complete solution method is characterized by fully centred spatial discretization with an accuracy of $O(h^3)$ for the velocity.

3.4. *Second-order BDF projection method*

Second-order accuracy in time can be achieved by replacing the first-order backward Euler scheme considered in (3.3) by a second-order-accurate time-stepping algorithm. Here, the three-level BDF is chosen because it benefits from better stability properties than those of the often used Crank–Nicolson scheme, which is known to be only marginally stable. The unconditional stability is maintained in the nonlinear regime by using the skew-symmetric form of the advection term evaluated semi-implicitly by approximating the advection velocity at the new time level by means of the linear extrapolation in time:

$$\boldsymbol{u}_\star^{k+1} = 2\boldsymbol{u}^k - \boldsymbol{u}^{k-1}. \tag{3.7}$$

For the first step $k = 0$, the velocity $\boldsymbol{u}^1$ and the pressure p^1 are calculated by means of the incremental projection method based on the Euler time stepping described in § 3.2.

For any subsequent time step with $k \geqslant 1$ the three-level BDF time stepping is employed. This means that the equation of the viscous step is integrated by the second-order-accurate BDF scheme:

$$\left.\begin{aligned} &\frac{3\boldsymbol{u}^{k+1} - 4\boldsymbol{u}^k + \boldsymbol{u}^{k-1}}{2\Delta t} - \nu\nabla^2\boldsymbol{u}^{k+1} + (\boldsymbol{u}_\star^{k+1} \cdot \nabla)\boldsymbol{u}^{k+1} + \tfrac{1}{2}(\nabla \cdot \boldsymbol{u}_\star^{k+1})\boldsymbol{u}^{k+1} \\ &\qquad = -\begin{cases} \nabla(3p^1 - 2p^0) & \text{for } k = 1 \\ \frac{1}{6}\nabla(14p^2 - 11p^1 + 3p^0) & \text{for } k = 2 \\ \frac{1}{3}\nabla(7p^k - 5p^{k-1} + p^{k-2}) & \text{for } k \geqslant 3 \end{cases} \\ &\boldsymbol{u}^{k+1}{}_{|\partial\Omega} = \boldsymbol{b}^{k+1}. \end{aligned}\right\} \tag{3.8}$$

Then, the projection step of the BDF incremental method is performed as follows:

$$\left.\begin{aligned} -\nabla^2(p^{k+1}-p^k) &= -\frac{3}{2\Delta t}\,\nabla\cdot\boldsymbol{u}^{k+1}, \\ \frac{\partial(p^{k+1}-p^k)}{\partial n}_{|\partial\Omega} &= 0. \end{aligned}\right\} \tag{3.9}$$

The two special expressions for pressure extrapolation for $k = 1$ and $k = 2$ are due to elimination of the first end-of-step velocity by means of the special relation of the first incremental projection step.

The BDF scheme was proved to be second-order accurate in time by Guermond (1999). It is the weak form of this algorithm using the spatial discretization described above that is implemented in the finite element code.

3.5. *Numerical implementation*

At each time step, the discrete counterparts of (3.8) and (3.9) amount to solving four linear systems of equations. All these systems are solved by preconditioned iterative techniques from the SPARSKIT Package of Youcef Saad.

In the computations reported below, we have used a non-uniform mesh composed of $5 \times 39^2 \times 30$ P_1-P_2 tetrahedra for the half-cavity ($\approx 300\,000$ P_2 nodes). In all the experiments described above, the flow has been observed to be symmetric with respect to the plane $z = 0$. This has also been verified numerically by Chiang, Hwang & Sheu (1997). Therefore, we have assumed the symmetry in our numerical simulations. Accordingly, the distributions of the nodes is

$$\left.\begin{aligned} x_i, y_i &= \tfrac{1}{2} + \tfrac{1}{2}\cos\left(\pi\frac{i-1}{I-1}\right),\ 1 \leqslant i \leqslant I, \\ z_j &= \sin\left(\frac{\pi}{2}\,\frac{j-1}{J-1}\right), 1 \leqslant j \leqslant J. \end{aligned}\right\} \tag{3.10}$$

The mesh $\mathscr{T}_h$ is obtained from the Cartesian grid by dividing each cell into five tetrahedra. The size of the tetrahedra located on the boundary in the direction normal to the walls is 1.9×10^{-3}, and the distance of the nodes nearest to the wall is less than 9×10^{-4} from the wall.

To enforce the velocity boundary conditions, there are two possibilities in the treatment of the nodes along the intersection of the moving wall with the upper and lower walls. If we set $u_x = -1$ at these nodes, then we allow a very small inflow and a corresponding outflow. The other possibility consists in setting the velocity to be zero on the nodes in question. In mathematical terms, this choice corresponds to a quadratic regularization confined within the elements located along the aforementioned intersection edges. We have tried both procedures and the projection method described above produces virtually indistinguishable results on the meshes considered, except for the case of the perturbed flows to be described in § 5.

To assess the accuracy of the numerical solution, we have also employed a non-uniform mesh composed of 5×30^3 tetrahedra for the half-cavity ($\approx 200\,000$ P_2 nodes) and we have compared the results to those obtained by means of the refined mesh. We computed the local errors of the velocity components u_x and u_y along the horizontal ($x = \frac{1}{2}$) and vertical ($y = \frac{1}{2}$) centrelines in the three planes $z = 0$, $z = \frac{1}{2}$ and $z = \frac{3}{4}$ for times $t = 2, 4, 6, 8, 10, 12$. The maximum value of all these local errors is found to be 1.2%. This comparison of the solutions on the two meshes indicates that the boundary layers for the Reynolds number considered is adequately resolved.

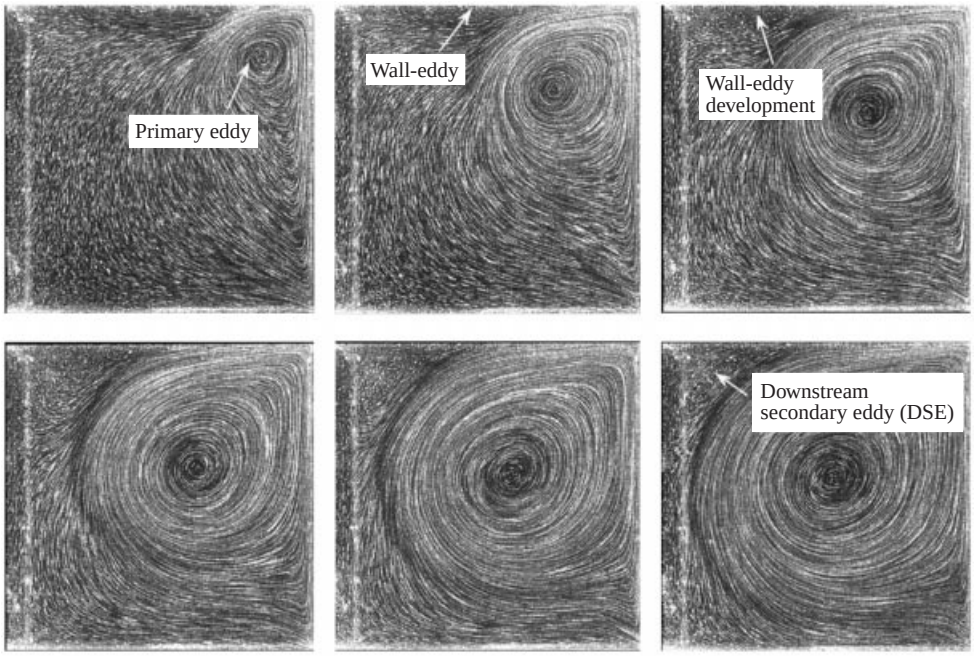

FIGURE 6. Visualization of the flow evolution by the particle-streak technique at times $t = 2, 4, 6, 8, 10, 12$ (from left to right and top to bottom) in the symmetry plane $z = 0$.

The computations have used $\Delta t = 0.01$ for the coarse mesh and $\Delta t = 0.004$ for the finer one. The simulations and the experiments are carried out from $t = 0$ to $t = 12$, a limit imposed by the vertical extent of the experimental equipment. To verify that the conditions for the flow at $t = 12$ have reached a quasi-stationary state, we have carried out the calculations (for the unperturbed flow) up to time $t = 18$. The comparison of the solutions at times $t = 12, 14, 16, 18$ indicates that the entire start-up phase of the flow was nearly completed at $t = 18$.

4. Comparisons for the unperturbed flow

4.1. *General flow description*

In this section, we give a general topological description of the unperturbed flow development both in cross-sections and span-sections. Quantitative comparisons between experiments and calculations of topological and kinematics data are presented in § 4.2, § 4.3, and § 4.4.

We consider first the time-evolution of the flow in cross-sections. In figure 6 we show a temporal sequence of experimental visualizations performed in the symmetry plane $z = 0$ by using the particle-streak method. Similar flow developments are observed in the other two selected planes $z = \frac{1}{2}$ and $z = \frac{3}{4}$.

The initial velocity field is zero in the entire cavity. As soon as the lid is set in upward motion, high shear stress develops along the cavity lid. Dragged to the upper right corner and deflected by the upper wall, the high velocity fluid penetrates the quiescent fluid region in the form of a counter-clockwise-rotating primary structure initially located close to the upper right corner. As time increases, the primary

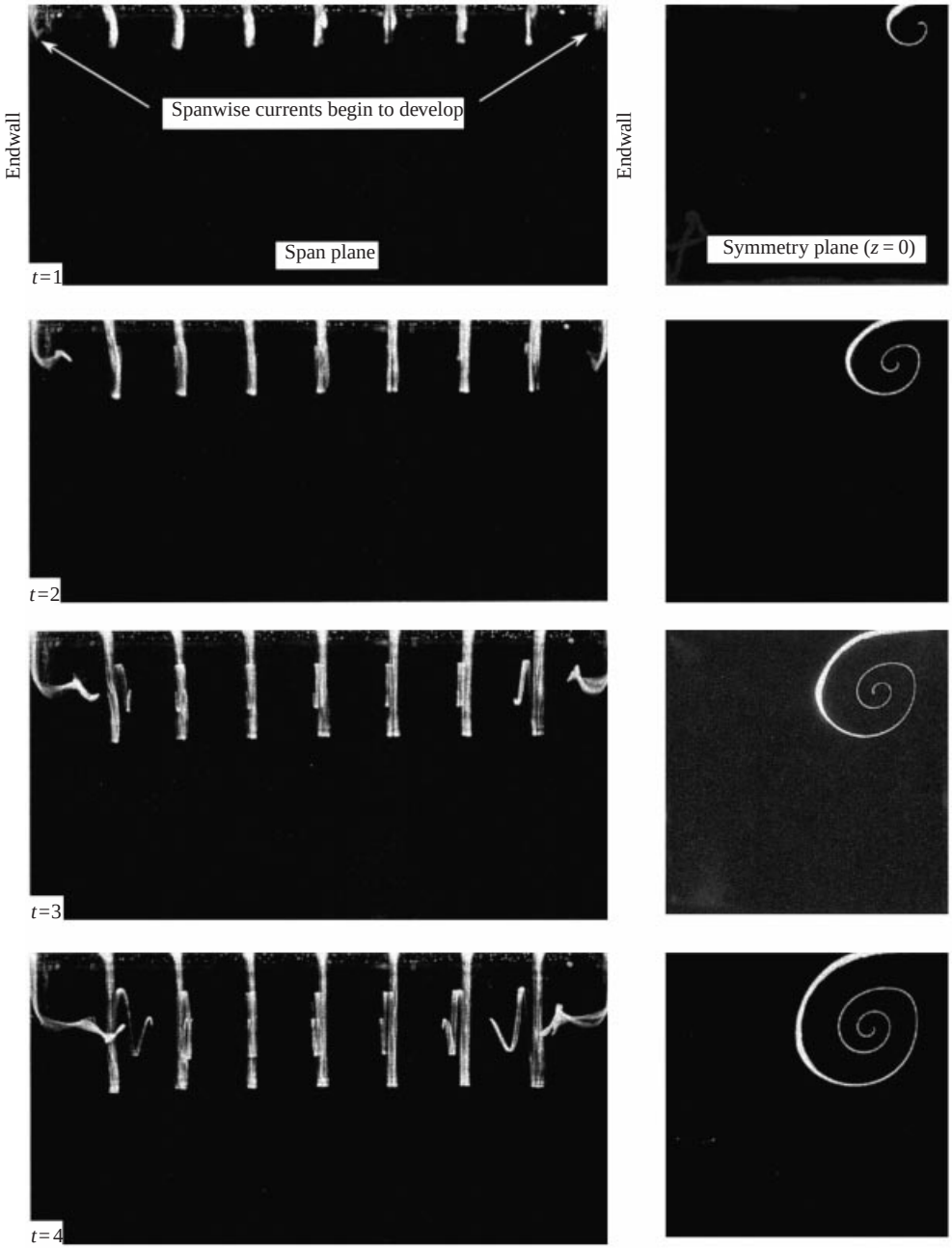

FIGURE 7. Visualization of the flow evolution by the dye-emission technique at times $t = 1, 2, 3, 4$. (*a*) Dye-filaments viewed from the y-direction. (*b*) Visualization in the symmetry plane $z = 0$; only the central tin ribbon is switched on and the light sheet illuminates the plane $z = 0$,

structure grows and moves towards the cavity centre as shown in figure 6 (see also § 4.3 for quantitative information).

From $t \approx 4$, an additional clockwise-rotating secondary eddy appears at the mid-height of the upper wall. For $t > 4$, this wall-eddy grows and moves towards the upper

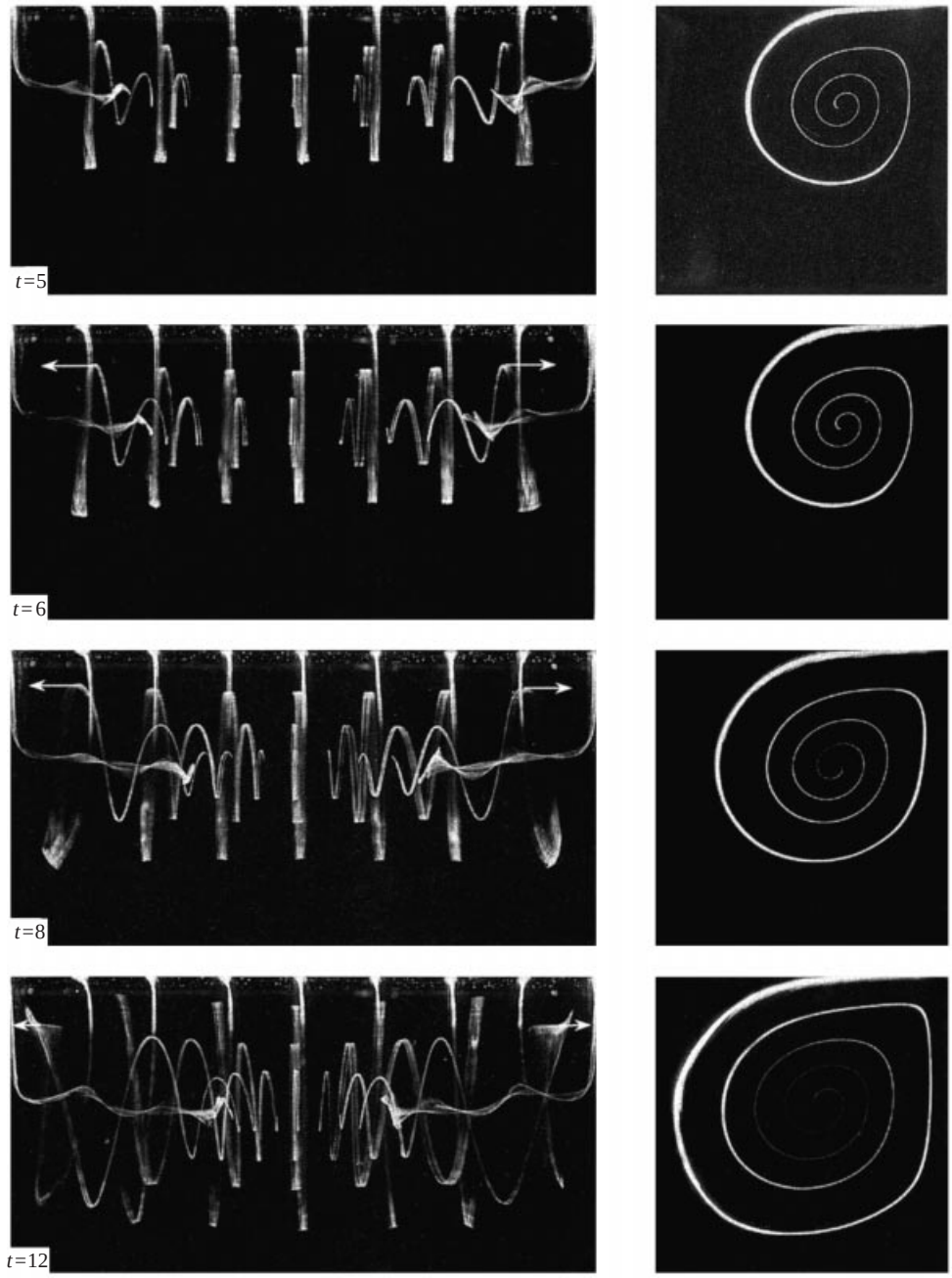

FIGURE 8. As figure 7 but at times $t = 5, 6, 8, 12$.

left corner, and ultimately evolves to form the downstream secondary eddy (DSE) in the established flow. Up to $t = 12$, we observe the formation of neither the upstream secondary eddy (USE) nor the lower secondary eddy (LSE) in both experiments and calculations. These eddies develop at times greater than 12.

Due to the no-slip condition at the endwalls, a spiral motion is superposed onto the cylindrical 'motion associated with the primary eddy. To illustrate this phenomenon,

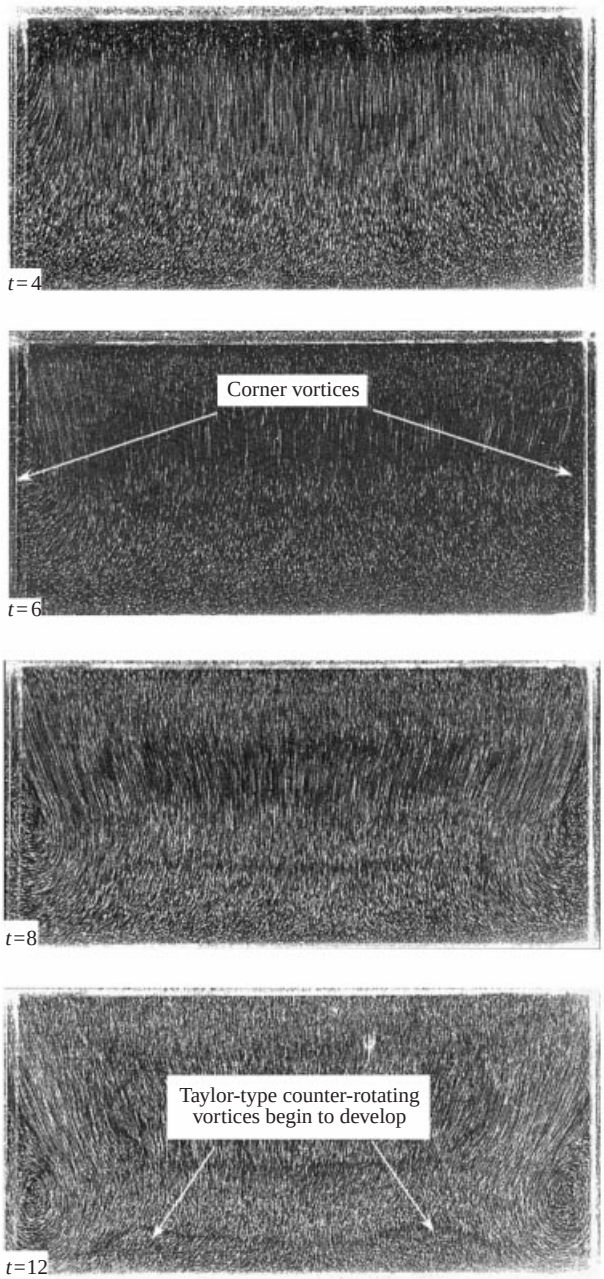

FIGURE 9. Time evolution of the flow in the plane $y = \frac{1}{2}$ visualized with the particle-streak method.

temporal sequences of emission lines in the symmetry plane $z = 0$ and spanwise views from the half-space $y > 1$ are shown in figures 7 and 8. In this experiment, the nine tin ribbons generating the emission lines are buried in the wall $x = 0$, and the wall is finely polished, for reasons to be explained in § 5.1.

In the symmetry plane, the dye penetrates the cavity in the form of a regular rounded rolling-up filament depicting the mixing process inside the primary eddy. With time increasing, the filament progresses regularly, keeping a quite rounded shape. In the

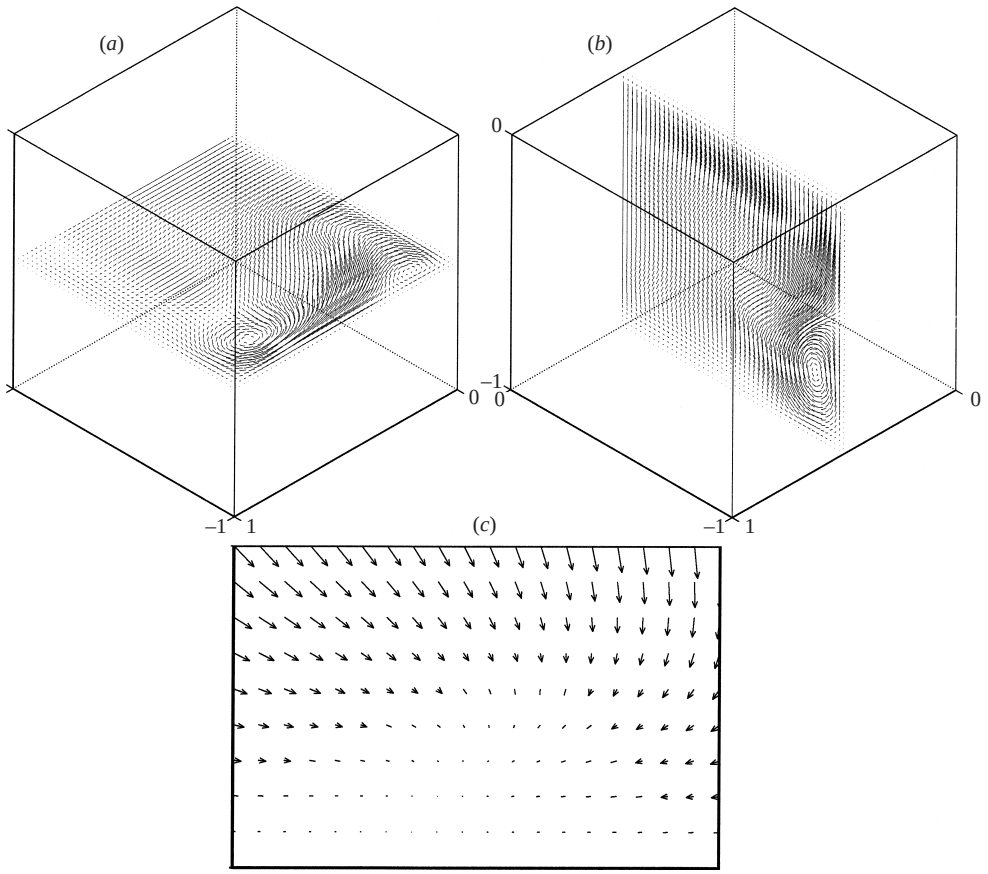

FIGURE 10. Evidence of the early formation of a Taylor-type counter-rotating pair of vortices. Velocity fields at $t = 12$ in the half cavity $z \in [-1,\ 0]$. (a) Velocity field in the horizontal plane $x = \frac{1}{2}$; (b) Velocity field in the vertical plane $y = \frac{1}{2}$; (c) Enlargement of the second view in region $z \in [-0.575, -0.4], x \in [0.9, 1]$.

span view, at $t = 1$, each filament rolls-up within its emitting section, indicating the two-dimensional character of the initial flow. However, from $t = 1$ and more noticeably from $t = 2$, the three-dimensionality of the flow starts to be visible close to the two endwalls as the filaments begin to develop axially towards the symmetry plane. These two opposite inward currents result from the interaction between the primary eddy and the viscous damping effects of the endwalls: a negative spanwise pressure gradient is induced from the endwalls towards the symmetry plane (Chiang *et al.* 1997). At later times, the dye filaments progress towards the symmetry plane, successively crossing all the emitting sections up to the symmetry plane. The initial two-dimensional roll-up of each filament then develops in the spanwise direction in the form of a spiral having a cone-shaped structure. At sections $z = \frac{3}{4}$, $\frac{1}{2}$, and $\frac{1}{4}$ the flow loses its two-dimensional character at times $t \approx 3$, 4, and 5, respectively. At $t = 6$, the whole cavity is affected by the three-dimensional spanwise motion. The filament in the plane $z = 0$ develops two-dimensionally up to the final time $t = 12$, indicating that the flow is symmetric with respect to this plane. Note however that for $t \geqslant 6$ the flow in the symmetry plane is different from the purely two-dimensional one, for spanwise shear effects are no longer negligible, see Migeon (2000).

Also of note from the spanwise visualizations in figure 8 is the peripheral outward current that moves the fluid towards the endwalls. This current is active in the periphery of the primary eddy in the manner indicated by a white arrow in the pictures.

The dye-emission technique visualizes the dynamics of the global three-dimensionality of the flow, but does not provide information on local eddies located near the endwalls nor on global eddies distributed along the cavity span. The temporal and spatial development of these structures can be visualized by means of the particle-streak technique. In figure 9 we present visualizations in the vertical plane $y = \frac{1}{2}$ at times $t = 4, 6, 8, 10$. It is clear that the flow is symmetric with respect to the plane $z = 0$. At time $t = 6$, we notice the formation of two corner vortices close to the mid-height of the two endwalls. As time increases, each corner vortex grows and moves towards the corners formed by the endwall and the lower wall. This corner vortex is also observed in plane $y = \frac{1}{4}$ (near the corner between the endwall and the upper wall) and two traces of the vortex are visible in the plane $x = \frac{1}{2}$ (one near the lid wall and the other near the left wall). This implies that this corner vortex has a 'banana shape'. A detail description of corner vortex development is beyond the scope of the present paper. Precise information about their development can be found in Chiang *et al.* (1997).

Starting from $t = 10$ there is evidence that two counter-rotating pairs of vortices start developing symmetrically in the plane $y = \frac{1}{2}$ close to the spanwise location $z = \pm\frac{1}{2}$. However, no fully developed counter-rotating motion can be observed before $t = 12$. This phenomenon is reproduced by the numerical simulation, as can be seen in the figure 10 which shows the velocity fields in the horizontal $y = \frac{1}{2}$ and vertical $x = \frac{1}{2}$ planes at $t = 12$ in the half-cavity $z \leqslant 0$. In this figure an enlargement of the numerical velocity field (u_x, u_z) in the plane $y = \frac{1}{2}$ in the region $0.9 \leqslant x \leqslant 1$ and $-0.575 \leqslant z \leqslant -0.4$ is also shown. Only the early stage of formation of the vortex pairs is detected from the characteristic undulation of the streamlines visualized in the fourth picture of figure 9. This structure is very localized in space since it has been observed only in span vertical planes but not in horizontal ones. We note also that it occurs in a region where the primary eddy is not yet separated, implying that the instability is not induced by a separation and seems to belong to the class of Taylor–Couette-type instabilities.

4.2. *Velocity profiles*

We now compare the velocity profiles along the horizontal ($x = \frac{1}{2}$) and vertical ($y = \frac{1}{2}$) centrelines in the three planes $z = 0$, $z = \frac{1}{2}$ and $z = \frac{3}{4}$, in figures 11, 12 and 13, respectively. On the horizontal centreline we have plotted $-\frac{1}{2}u_x$ versus $\frac{1}{2} - y$, whereas on the vertical centreline we have plotted $-\frac{1}{2}u_y$ versus $\frac{1}{2} - x$. This representation is classical for the two-dimensional driven cavity problem. For each figure we have reported the velocity at times $t = 4, 6, 8, 10, 12$.

The evolution of the velocity distributions is quite similar in the three planes considered, and the comparison between them indicates that three-dimensionality plays a limited role during the start-up phase. Globally, the development of the flow in the experiment and in the numerical simulation is seen to be very similar to each other for all planes and all times. In each plane, the differences between experiments and calculations are greater at later times $t = 10$ and $t = 12$ and are found to be located in the peripheral region of the primary eddy. The maximum disagreement is found to occur in the plane $z = \frac{1}{2}$.

We have found that slightly modifying the way the lid is numerically accelerated

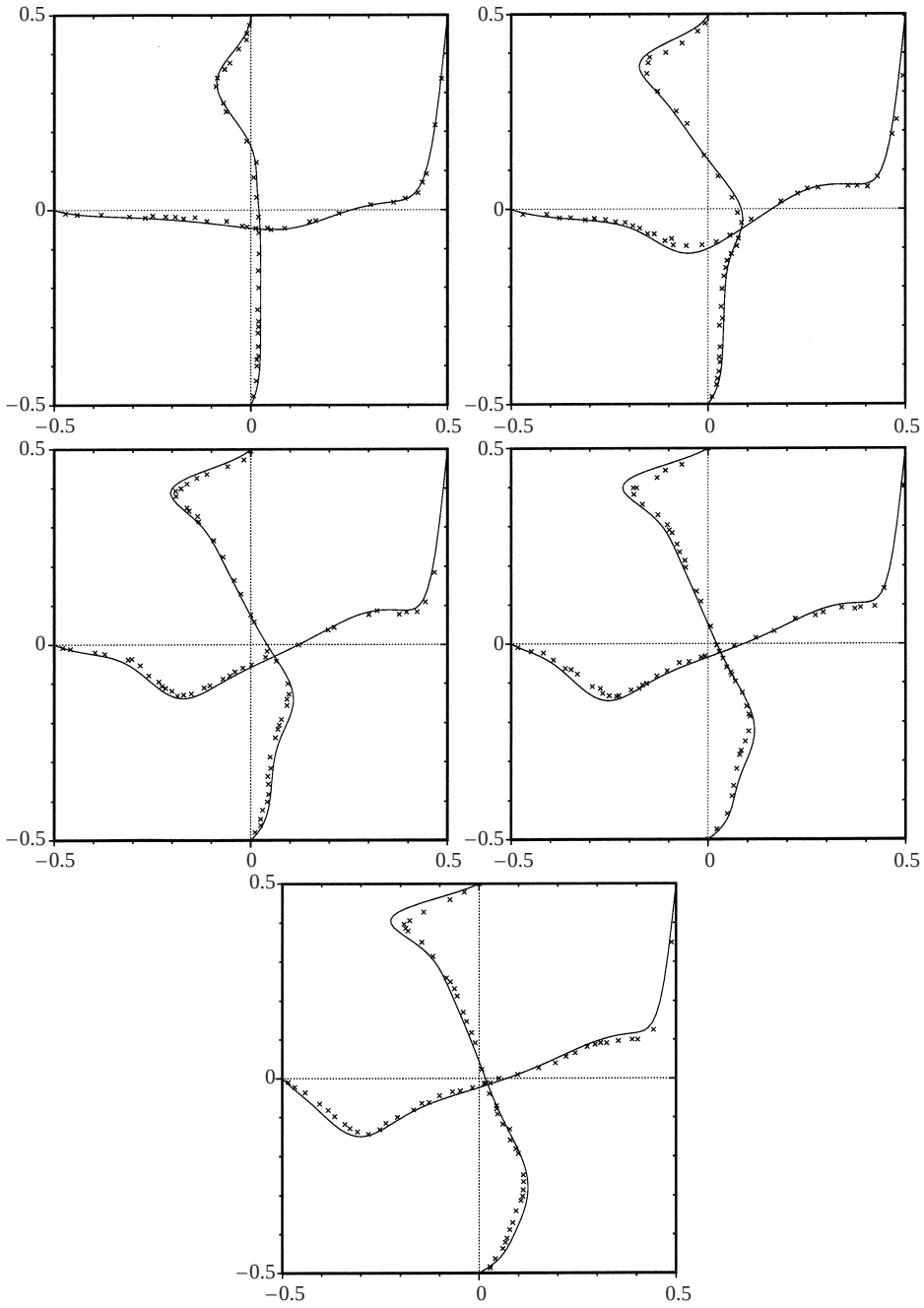

FIGURE 11. Velocity profiles in the symmetry plane $z = 0$ at times $t = 4$, 6, 8, 10, 12 (from left to right and from top to bottom). $-\frac{1}{2}u_x$ as a function of $\frac{1}{2} - y$ and $-\frac{1}{2}u_y$ as a function of $\frac{1}{2} - x$.

to reach the final velocity affects the velocity profiles up to time $t = 12$, especially in the region where the flow is the most unstable, i.e. in the USE region (see figure 1 for nomenclature). The conclusion of our numerical investigations is that a great part of the discrepancies observed between the measurements and the simulations can be attributed to the uncertainty in the acceleration law of the carriage.

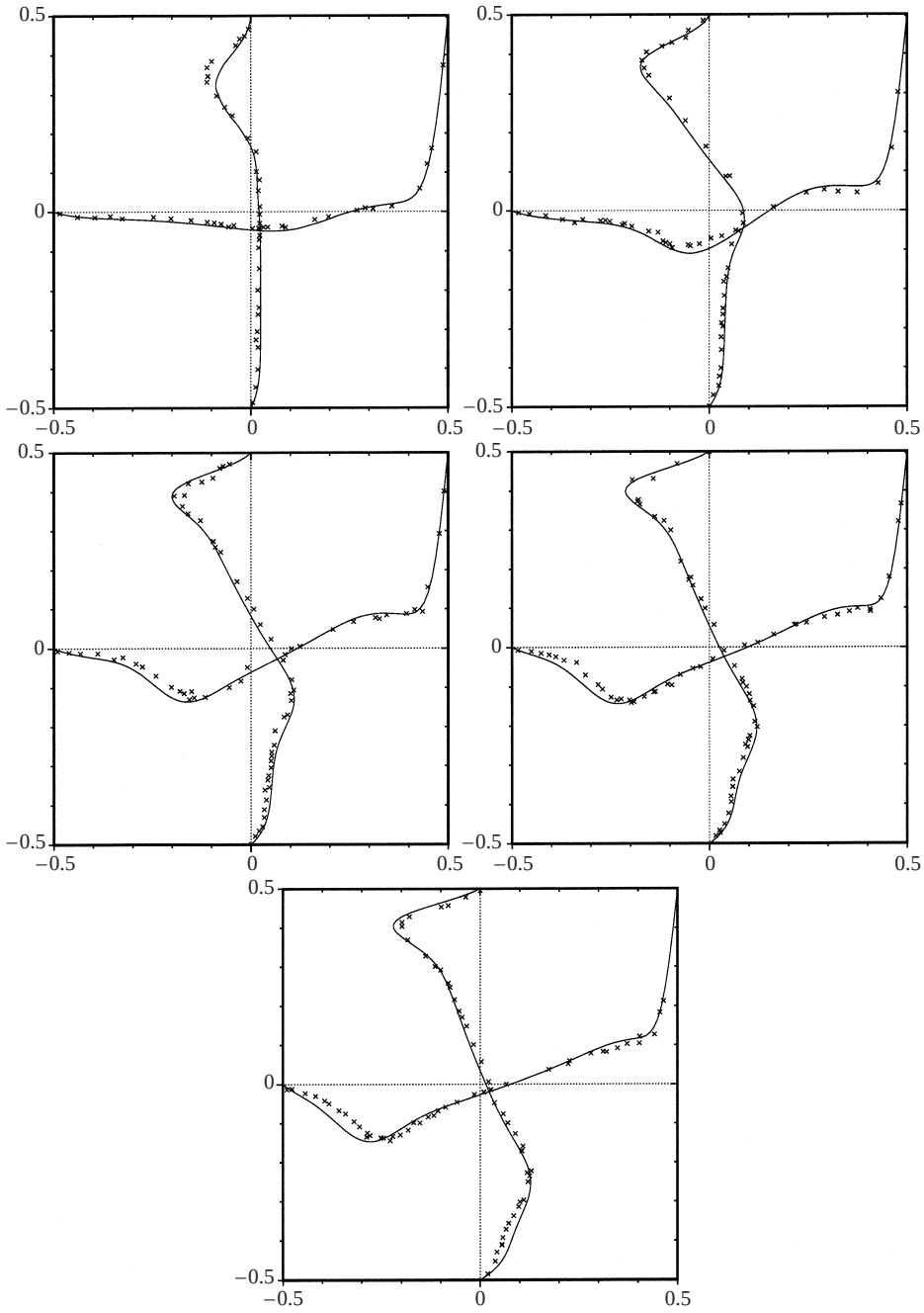

FIGURE 12. As figure 11 but in the plane $z = \frac{1}{2}$.

4.3. *Position of primary and secondary eddies*

In this section we make comparisons between the experiments and the computations on the position of the primary eddy and the position of the downstream secondary eddy. These data are considered a 'useful benchmark' for result comparisons in Koseff & Street (1984*c*). In the experiment, the eddy position and dimensions are measured

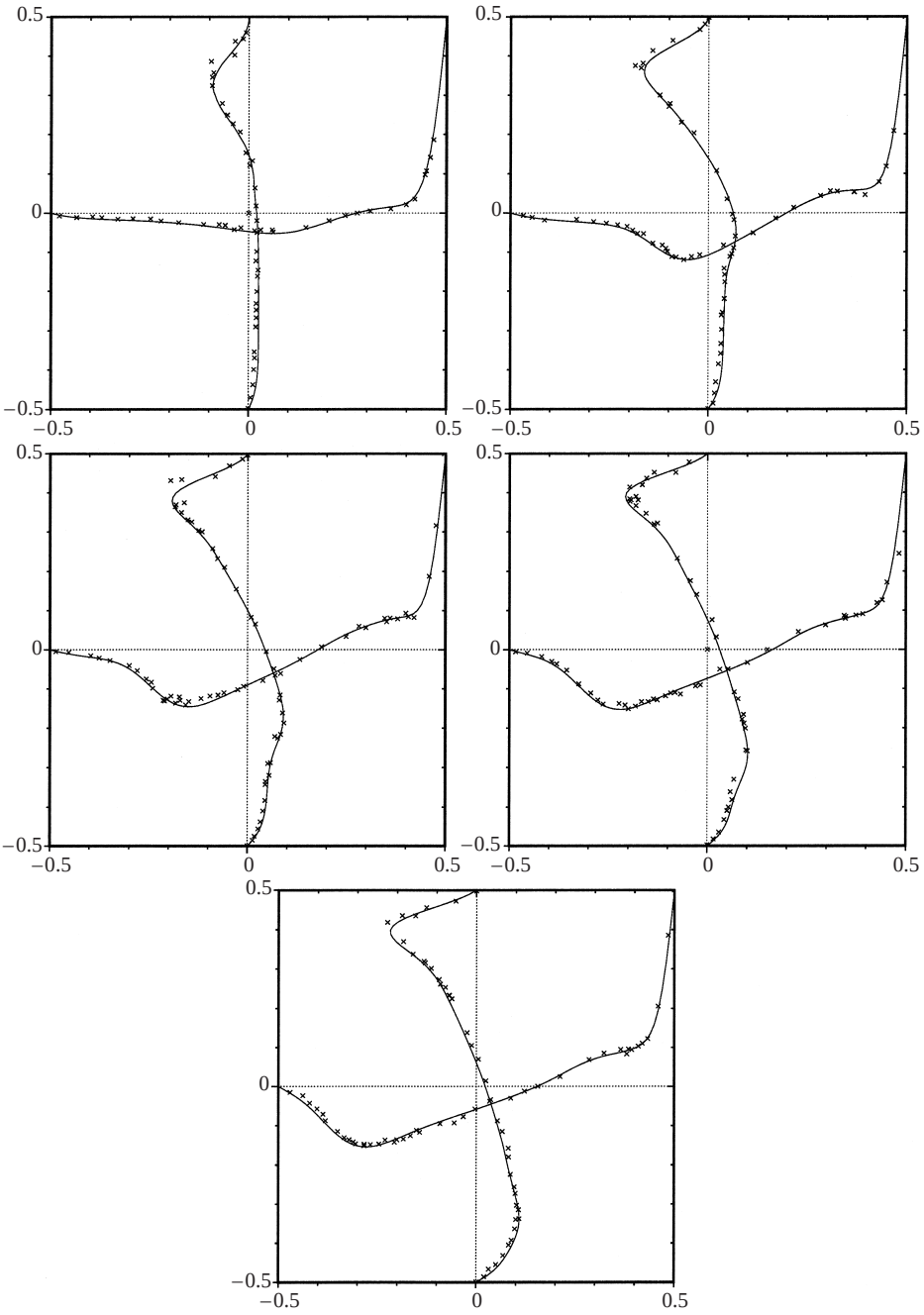

FIGURE 13. As figure 11 but in the plane $z = \frac{3}{4}$.

from particle-streak visualizations. We denote by D_x (resp. D_y) the dimensionless distance between the separation (resp. reattachment) point of the downstream secondary eddy and the upper left corner of the cavity (i.e. $x = 0$, $y = 1$). We hereafter refer to (D_x, D_y) as the dimensions of the secondary eddy. In the computation, we measured the position of the primary and secondary eddies by searching for the points where

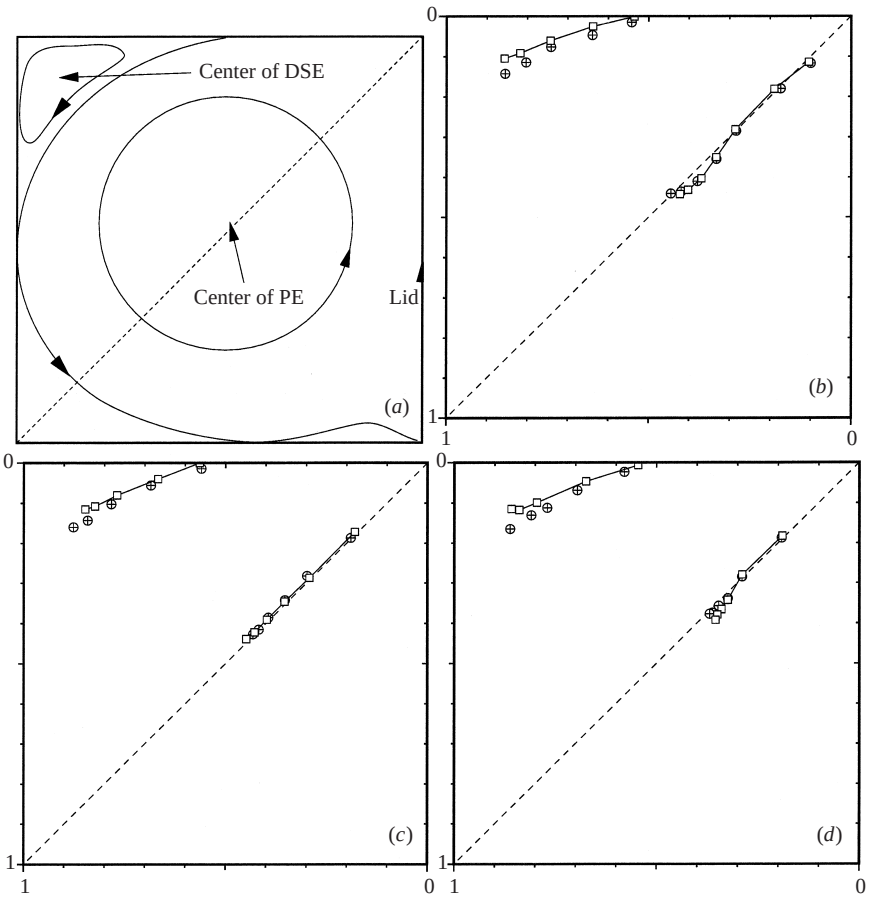

FIGURE 14. Position of the centre of the primary eddy and of the downstream secondary eddy in planes $z = 0$ (b), $z = \frac{1}{2}$ (c) and $z = \frac{3}{4}$ (d). The symbol $\square$ is for numerical results while $\oplus$ is for measurements. The primary eddy moves along the diagonal towards the centre; the secondary eddy evolves along the upper wall towards the upper left corner.

$u_x^2 + u_y^2$ is zero. The dimensions of the secondary eddy are also found by minimizing $u_x^2 + u_y^2$ in the vicinity of separation and reattachment points.

In figure 14, we have plotted the position of the primary eddy in the symmetry plane $z = 0$ for times $t = 1, 2, 4, 6, 8, 10, 12$, and in the planes $z = \frac{1}{2}$ and $z = \frac{3}{4}$ for times $t = 2, 4, 6, 8, 10, 12$; in the same figure the position of the secondary eddy for times $t = 4, 6, 8, 10, 12$ in the three planes considered is also reported. The agreement on the position of the primary eddy between the experiment and the computation is very good for all times and all planes. The maximum difference is of order 2% of the reference length and occurs at $t = 1$. The centre of the primary eddy moves along the diagonal from the intersection of the moving wall with the upper wall. Note that in the symmetry plane the trajectory of the main vortex centre deviates slightly from the diagonal for times $t \geqslant 6$. The experiment and the computation produce almost the same curved trajectory. We also notice a fair agreement for the retardation effect caused by the vertical endwalls on the motion of the primary eddy in planes $z = \frac{1}{2}$ and $z = \frac{3}{4}$.

Figure 14 also shows noticeable systematic differences in the position of the down-

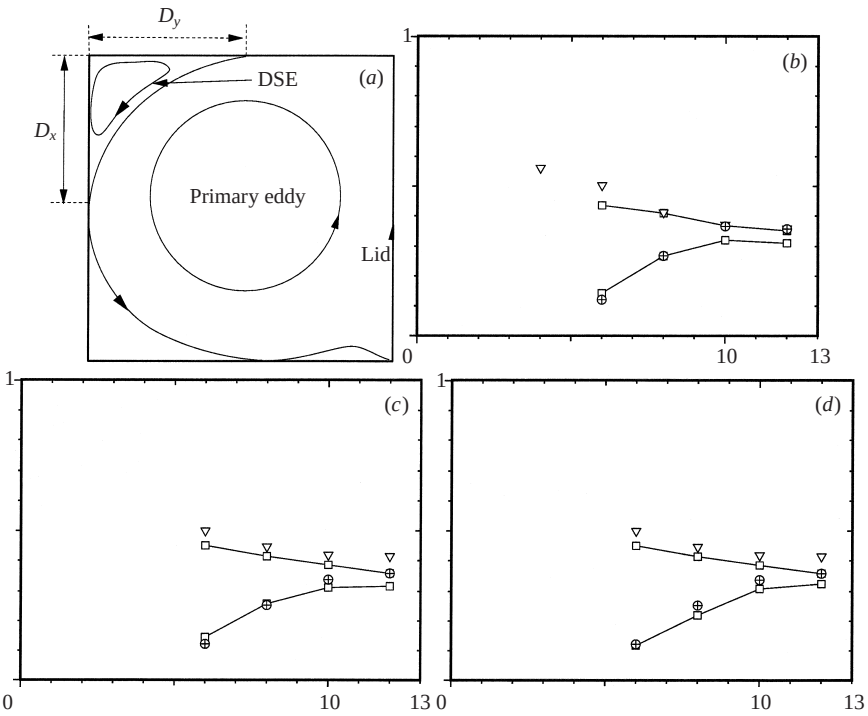

FIGURE 15. Dimensions of the downstream secondary eddy as a function of time in planes $z = 0$ (b), $z = \frac{1}{2}$ (c) and $z = \frac{3}{4}$ (d). The upper curve is for D_y and the lower one is for D_x. The symbol $\triangledown$ is for experimental D_y, $\oplus$ is for experimental D_x, and $\square$ is for numerical results.

stream secondary eddy. In the symmetry plane, greater differences are found on the x-coordinate than on the y-coordinate. More precisely, the discrepancy on the x-coordinate is of the order of 3.5% while that on the y-coordinate is less than 1.3%. For the two other planes, the maximum of the differences on the x and y positions is found to be of order 4% for time $t = 12$. For the three planes and all times, we observe that the numerical simulation predicts systematically that the eddy is slightly closer to the upper wall than in the experiment. We have no explanation for such a discrepancy.

4.4. *Dimensions of secondary eddies*

We now compare the experimental and numerical dimensions of the downstream secondary eddy, see figure 15(a) for the definition of D_x and D_y. The reattachment point moves left on the upper wall for $4 < t < 5$. It reaches the left wall at $t \approx 5$ and moves down the wall from this time. The numerical and experimental results are plotted in figure 15. Globally, the measured and computed positions of both the separation and reattachment points of the secondary eddy are in fair agreement for the three planes and times considered.

5. Comparisons for the perturbed flows

5.1. *Experimental evidence of perturbed flows*

During preliminary experiments, we used the electrolysis method by fixing tin ribbons on the surface of the upper wall very close to the moving wall. With this technique,

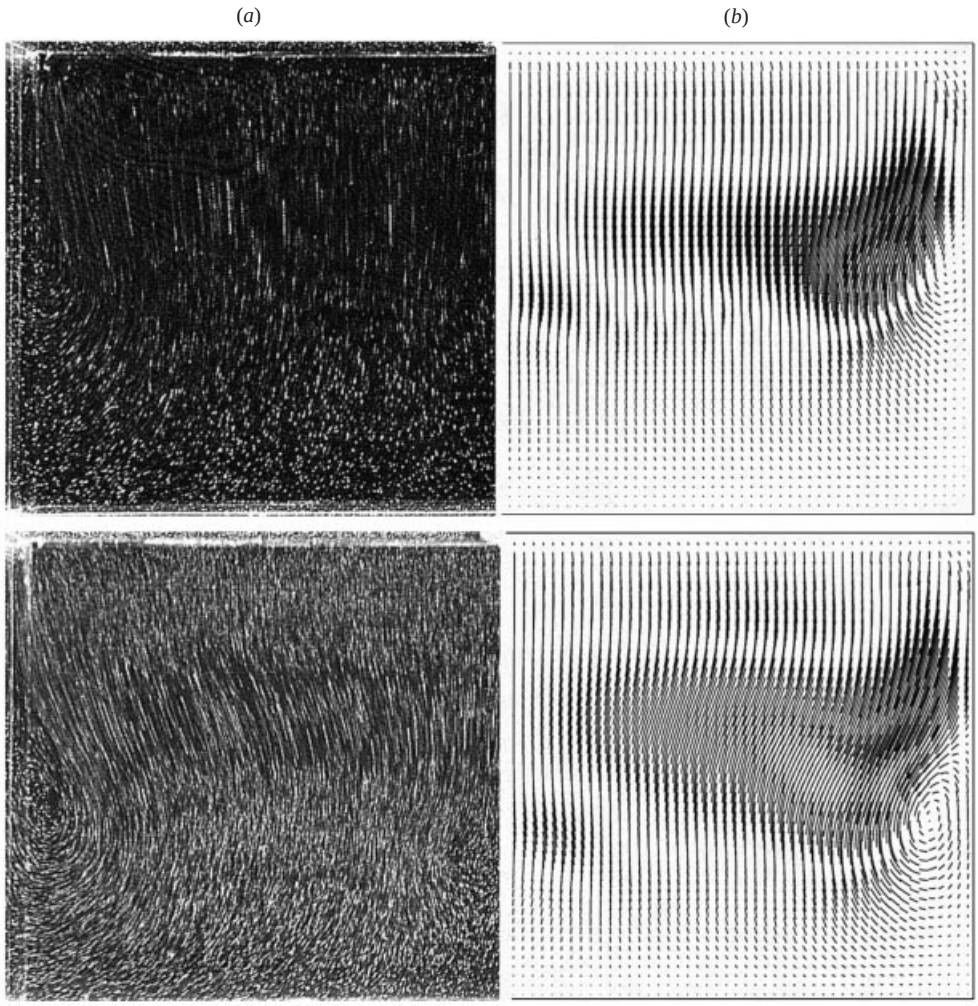

FIGURE 16. Cavity with one perturbation. Velocity field $(u_x,\ u_z)$ in the plane $y = \frac{1}{2}$ at times $t = 6$ and $t = 8$. (*a*) Experiment; (*b*) numerical simulation with $\epsilon = 1\%$.

we made two sets of measurements. In the first set, we glued only one ribbon at $z = 0$ to visualize the flow in the symmetry plane. In the second set, we tried to visualize the spanwise component of the fluid motion by glueing nine ribbons along the upper right edge of the cavity at uniformly distributed locations, as illustrated in figure 5. When we compared the filament shapes in the symmetry plane obtained in the two cases, we observed a great difference in the size of the areas occupied by the two filaments at given times. At this point, we could not explain the phenomenon because the active part of the tin ribbon in the cavity was so small that we assumed it to affect the flow field only marginally: each ribbon has roughly the shape of a parallepiped of dimensionless thickness $\delta x = 3.2 \times 10^{-3}$, length $\delta y = 0.081$ and width $\delta z = 0.032$. The experiments were conducted using tin ribbons of one fixed size, determined by the available materials.

To discover the origin of the differences, we used the particle-streak method while keeping the nine tin ribbons in the cavity without activating them. Then, we found that the flow field in the spanwise cross-section was dependent on the number of

(*a*) (*b*)

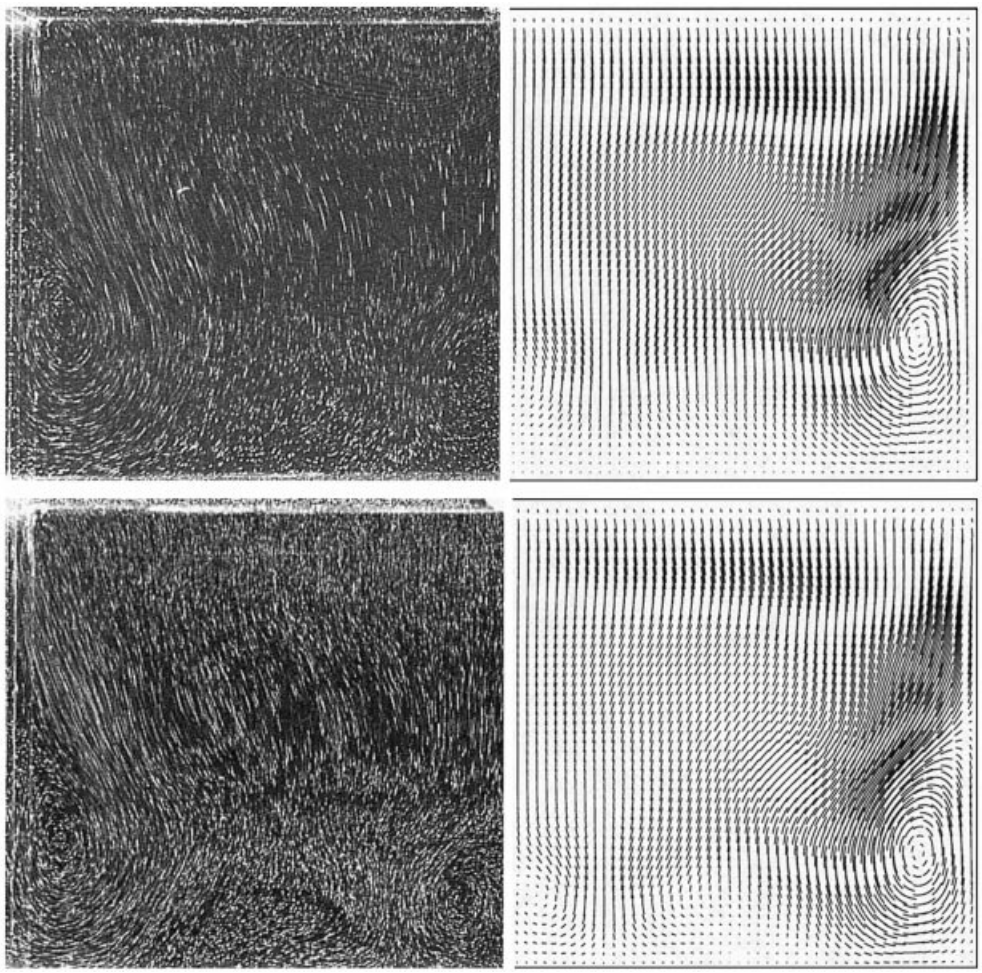

FIGURE 17. As figure 16 but at times $t = 10$ and $t = 12$.

ribbons present in the cavity and that it was quite different from the one observed in the absence of the ribbons. So we decided to make grooves in the upper wall to bury the tin ribbons into the altuglass and to polish the surface. The flow field observed afterwards was exactly the one obtained in the absence of ribbons.

The conclusion was that the flow is very sensitive to small perturbations located at the intersection of the lid and the upper wall. As a consequence we performed a series of different experiments with different numbers of unburied tin ribbons to obtain a quantitative appraisal of the effect of the perturbations.

In the following section we report on the flows we observed experimentally and describe the numerical procedure that has been used to simulate the flow in the presence of the unburied ribbons.

5.2. *Numerical perturbations of the cavity geometry*

The presence of the tin ribbons was reproduced numerically by modifying the shape of the cavity as follows. Two cases are considered hereafter: either we place one

ribbon across the symmetry plane or we place three ribbons, one in the symmetry plane and the other two across the planes $z = \frac{1}{2}$ and $z = -\frac{1}{2}$; the presence of the latter is a result of the assumed symmetry of the flow.

We have modified the upper wall of the cavity by introducing protuberances of the dimensions $\delta x = \epsilon$, $\delta y = 0.081$ and $\delta z = 0.032$, where ϵ is a small parameter to be selected later. The numerical protuberances of the boundary are obtained as follows.

First the distribution of nodes in the z-direction is generated according to the relation

$$z_j = \frac{1}{2}\left[1 - \cos\left(\pi \frac{j-1}{J-1}\right)\right], \quad 1 \leqslant j \leqslant J,$$

if only one tin ribbon is present in the cavity, and according to

$$z_j = \begin{cases} \dfrac{1}{4}\left[1 - \cos\left(2\pi \dfrac{j-1}{J-1}\right)\right], & 1 \leqslant j \leqslant \dfrac{J+1}{2}, \\ \dfrac{1}{4}\left[3 + \cos\left(2\pi \dfrac{j-1}{J-1}\right)\right], & \dfrac{J+1}{2} \leqslant j \leqslant J, \end{cases}$$

if there are three ribbons. This type of node distribution implies that the mesh is refined in the vicinity of planes $z = 0$, $z = \frac{1}{2}$ and $z = 1$.

Second, we create the mesh of the cubic cavity, as explained in § 3.5. Then, we displace the nodes, only in the x-direction, according to the following law:

$$x_{\text{new}} = \begin{cases} \epsilon + (1-\epsilon)x & \text{if } y \leqslant \delta y \quad \text{and} \quad z \leqslant \frac{1}{2}\delta z, \\ x & \text{otherwise} \end{cases}$$

for the case of a single ribbon, and

$$x_{\text{new}} = \begin{cases} \epsilon + (1-\epsilon)x & \text{if } y \leqslant \delta y \quad \text{and} \quad (z \leqslant \frac{1}{2}\delta z \text{ or } |z - \frac{1}{2}| \leqslant \frac{1}{2}\delta z), \\ x & \text{otherwise} \end{cases}$$

for the case of three ribbons. As a consequence of this simple definition of the geometric perturbation, the numerical protuberance is no longer parallepipedic. In fact, the faces that should be normal to the upper wall at $x = 0$ are actually oblique planes, thus producing a geometrical perturbation less sharp than in the experiment. We have compensated for this effect by using $\epsilon = 1\%$ or $\epsilon = 3.5\%$ in the case of one protuberance, and $\epsilon = 3.5\%$ in the case of three. Thus, the value of ϵ is three to ten times larger than the thickness of the experimental tin ribbon. Moreover, we have found that the perturbation is strong enough to trigger the early development of spanwise modes observed in the experiment only if we impose the value -1 on u_x at the nodes of the protuberance on the cavity edge. Due to the uncertainty in reproducing the experimental perturbation, we limit ourselves to preliminary comparisons.

5.3. *One perturbation*

In this section we describe the flow that is observed experimentally and numerically when only one tin ribbon is present in the cavity.

In figures 16 and 17, we show the flow development in the spanwise section $y = \frac{1}{2}$ for times $t = 6$, 8, 10, and 12. In part (*a*) we show the particle-streak visualizations and in part (*b*) the corresponding instantaneous numerical velocity field that is obtained with $\epsilon = 1\%$. The striking result is that one observes the formation of one Taylor-type

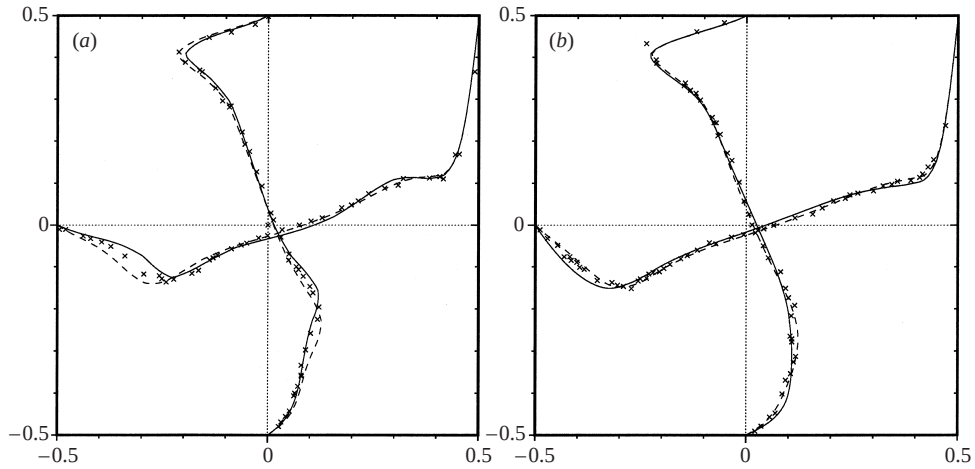

FIGURE 18. Cavity with one perturbation. Velocity profiles in the symmetry plane $z = 0$ (a) plane $z = \frac{1}{2}$ (b) at time $t = 12$; $-\frac{1}{2}u_x$ as a function of $\frac{1}{2} - y$ and $-\frac{1}{2}u_y$ as a function of $\frac{1}{2} - x$. Symbols correspond to experiments, dotted line corresponds to numerical perturbation $\epsilon = 0.01$ and solid line corresponds to numerical perturbation $\epsilon = 0.035$.

vortex pair across the symmetry plane. Note also that the size and the evolution of this vortex pair are quite well reproduced by the numerics.

In figure 18 velocity profiles at time $t = 12$ in planes $z = 0$ and $z = \frac{1}{2}$ are compared. Two computations have been made: one with a numerical tin ribbon of thickness $\epsilon = 1\%$ (dotted lines) and the other of thickness $\epsilon = 3.5\%$ (solid line). In both planes, wherever the two numerical profiles are found to be slightly different, the experimental data are contained within the domain delimited by the two numerical curves.

In figure 19 we show the velocity field $t = 12$ in the horizontal plane $x = \frac{1}{2}$ and in the vertical plane $y = \frac{1}{2}$. This pictures clearly show that the Taylor–Görtler vortex develops only in the USE region.

5.4. *Three perturbations*

We consider now the case of the flow perturbed by inserting three tin ribbons in the cavity. We performed numerical simulations with perturbations $\epsilon = 3.5\%$ and $\epsilon = 1.5\%$.

In figure 20, we compare the particle-streak visualizations of the flow and the numerical velocity field in plane $y = \frac{1}{2}$ at times $t = 6$, 8, and 10 (for $t = 12$ see figure 3). The time evolution of the spanwise modes is very similar in the experiment and the computation. In particular we notice that the positions of the centre of the four vortices are almost identical in the computation and the experiment. Note that Taylor–Görtler-like vortices were observed by Koseff & Street (1984a, b, c) in the horizontal plane, but in previous works there was no evidence of such structures in spanwise vertical planes.

In figure 21 we present views of the velocity field projected on the horizontal plane $x = \frac{1}{2}$ and vertical plane $y = \frac{1}{2}$ at $t = 12$. As in the case of one perturbation, these pictures show that the Taylor–Görtler-like vortices are localized in the USE region, confirming that this zone is prone to instabilities. Our experiments and numerical simulations clearly indicate also that the region in the vicinity of the intersection of the upper wall and the moving wall is highly sensitive to perturbations.

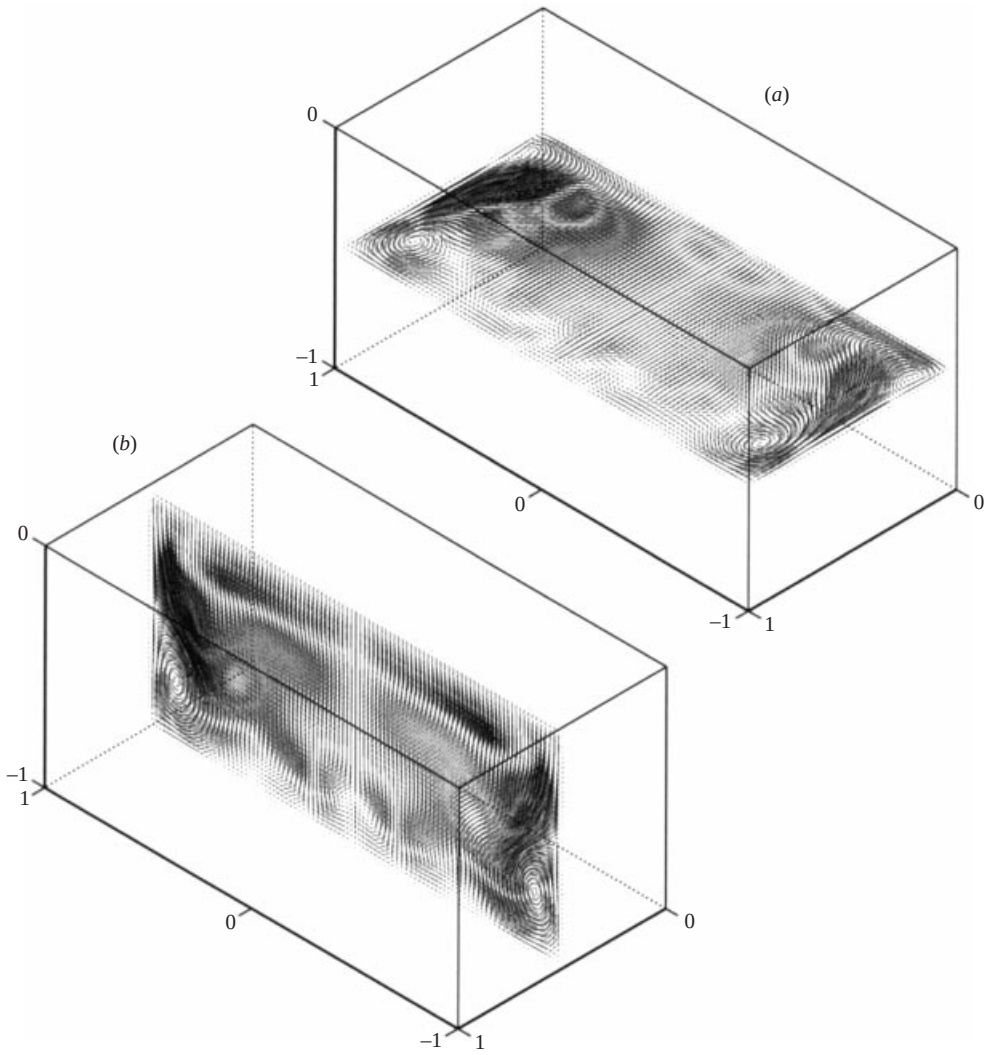

FIGURE 19. Cavity with one perturbation. Velocity field $(u_y,\ u_z)$ in the horizontal plane $x = \frac{1}{2}$ (a) and velocity field $(u_x,\ u_z)$ in the vertical plane $y = \frac{1}{2}$ (b) at time $t = 12$.

5.5. *On the nature of the instabilities*

To determine whether the boundary layer perturbations that we introduced artificially only affected the initiation process or had long-term effects, we performed additional numerical experiments. In the case of the flow with three perturbations, we continued the calculations up to $t = 24$, and we observed that the three Taylor–Görtler vortices did not show any tendency to disappear but seemed to reach some steady state. We performed a second experiment in which we used the velocity field obtained at $t = 12$ in the three perturbations case as the initial data for the unperturbed cavity. At $t = 24$ the three Taylor–Görtler vortices had almost disappeared, and the velocity field seemed to converge to the same steady state as that of the impulsively started unperturbed cavity. These two experiments indicate that the observed vortices are associated with a convective instability, though this classification may be misleading

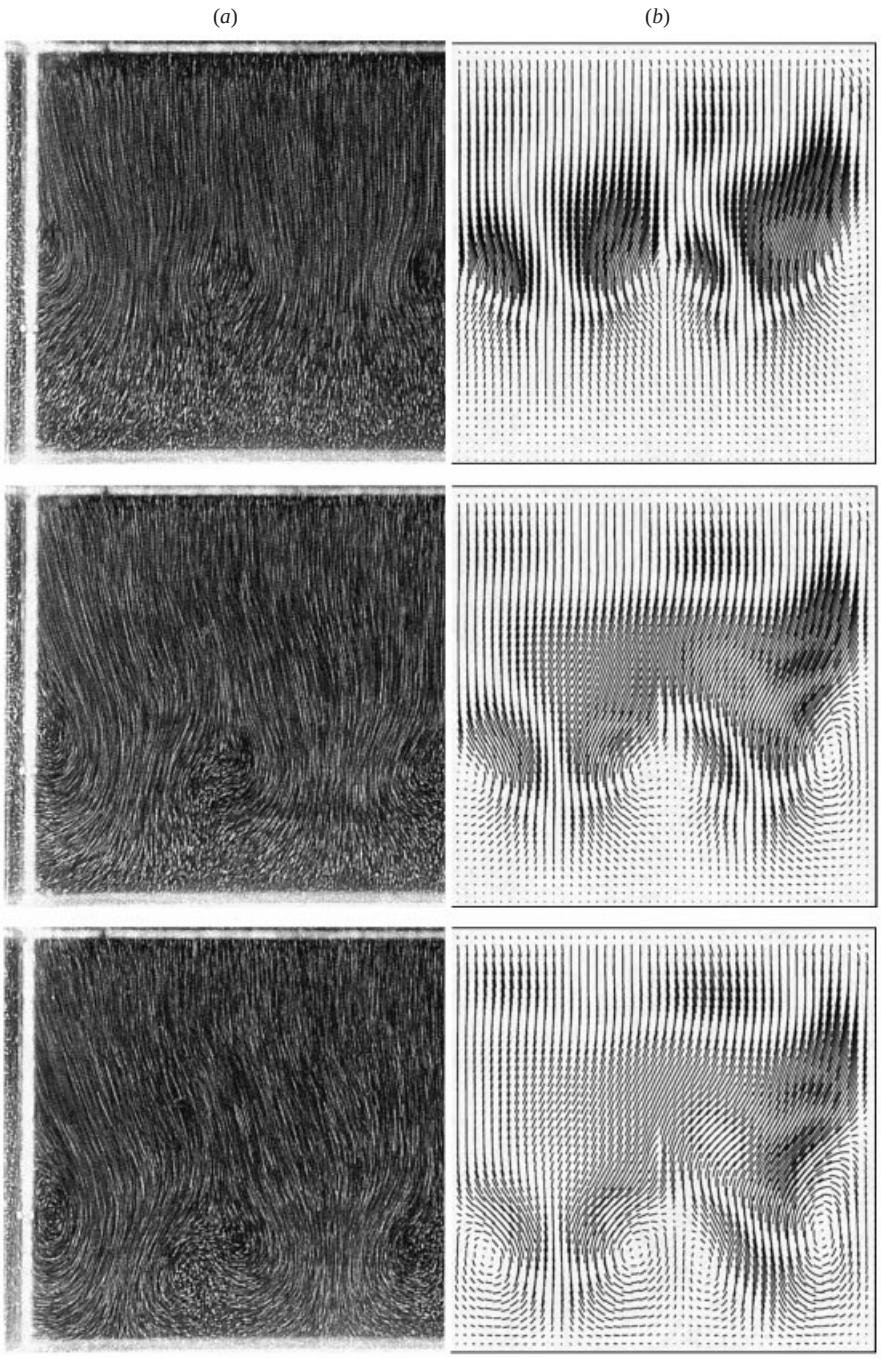

FIGURE 20. Cavity with three perturbations. Velocity field $(u_x,\ u_z)$ in the plane $y = \frac{1}{2}$ at times $t = 6$, 8, and 10, see figure 3 for $t = 12$. (a) Experiment, (b) numerical simulation.

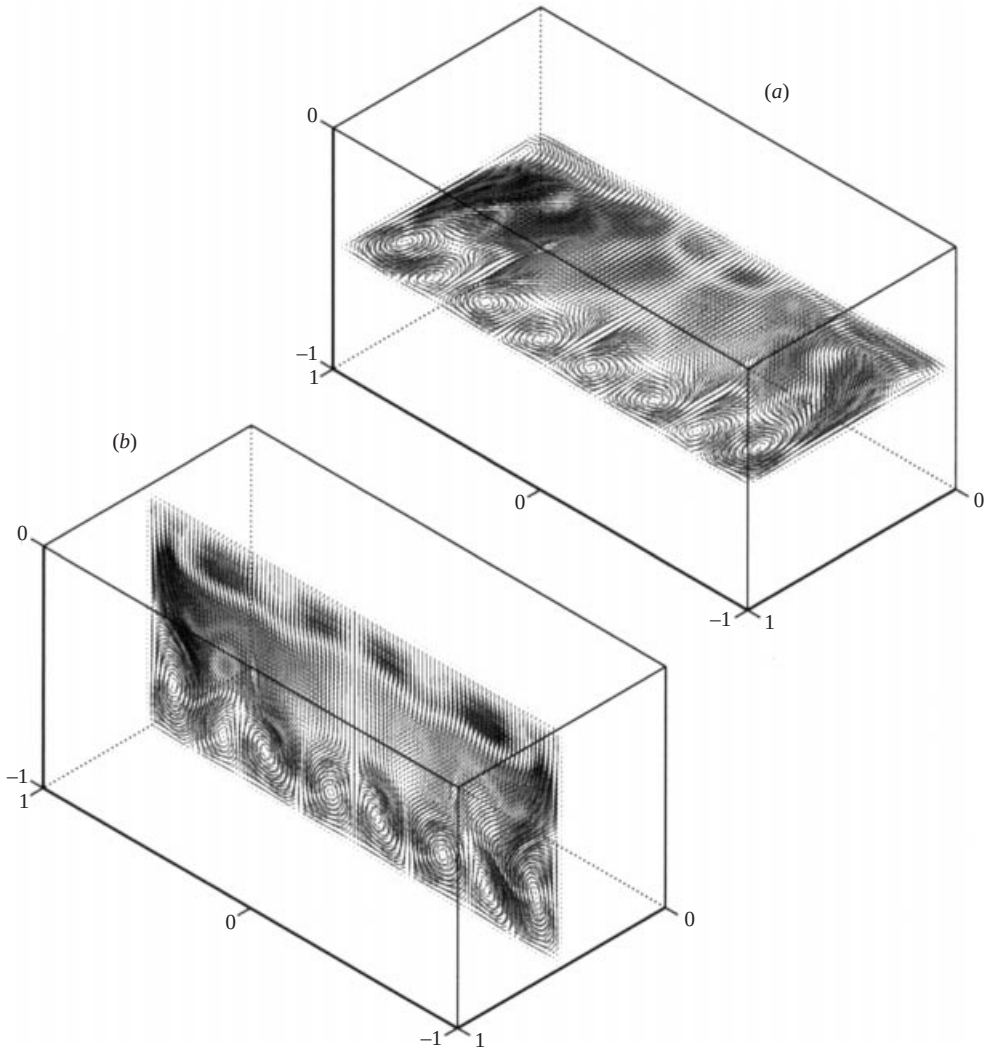

FIGURE 21. Cavity with three perturbations. Velocity field $(u_y,\ u_z)$ in the horizontal plane $x = \frac{1}{2}$ (a) and velocity field $(u_x,\ u_z)$ in the vertical plane $y = \frac{1}{2}$ (b) at time $t = 12$.

since the flow domain is bounded. As Görtler vortices are known to be convective instabilities, we are led to concluding that the observed vortices belong to the class of Görtler vortices.

6. Conclusions

Flows in enclosures at moderate Reynolds numbers are commonly considered to be simple fluid dynamics problems controlled by a very small number of parameters. In particular, viscous incompressible flows in three-dimensional rectangular regions were expected to provide canonical situations from both the experimental and numerical viewpoints, at least for Reynolds numbers in the range $Re \leqslant 1000$. Contrary to this expectation, the present paper shows that at $Re = 1000$, in the early stage of the start-up, three flow evolutions with completely different three-dimensional structures

are observed under tiny perturbations of the cavity geometry. This result is produced by the combined effects of three-dimensionality of the flow and the singular character of the lid-driven-cavity problem. Consequently, the predictability of three-dimensional incompressible viscous flows in bounded regions even at rather moderate Reynolds numbers requires a control of the boundary geometry and boundary conditions that is significantly strikingly more precise than needed in two-dimensional situations.

REFERENCES

Barragy, E. & Carey, G. F. 1997 Stream function–vorticity driven cavity solution using p finite elements. *Comput. Fluids* **26**, 455–468.

Boisaubert, N., Coutanceau, M. & Ehrman, P. 1996 Comparative early development of wake vortices behind a short semicircular-section cylinder in two opposite arrangements. *J. Fluid Mech.* **327**, 73–99.

Botella, O. & Peyret, R. 1998 Benchmark spectral results on the lid-driven cavity flow. *Comput. Fluids* **27**, 113–151.

Burggraf, O. R. 1966 Analytical and numerical studies of the structure of steady separated flows. *J. Fluid Mech.* **24**, 113–151.

Chiang, T. P., Hwang, R. R. & Sheu, W. H. 1997 On end-wall corner vortices in a lid-driven cavity. *Trans. ASME: J. Fluids Engng*, **119**, 201–204.

Chiang, T. P., Sheu, W. H. & Hwang, R. R. 1998 Effect of Reynolds number on the eddy structure in a lid-driven cavity. *Intl J. Numer. Meth. Fluids* **26**, 557–579.

Chorin, A. J. 1968 Numerical solution of the Navier–Stokes equations. *Math. Comput.* **22**, 745–762.

Chorin, A. J. 1969 On the convergence of discrete approximations to the Navier–Stokes equations. *Math. Comput.* **23**, 341–353.

Deville, M., Le, T.-H. & Morchoisne, Y. (Eds.) 1992 *Numerical Simulation of 3-D Incompressible Unsteady Viscous Laminar Flows*. Notes on Numerical Fluid Mechanics, vol. 36. Vieweg.

Fortin, A., Jardak, M., Gervais, J. J. & Pierre, R. 1997 Localization of Hopf bifurcations in fluid flow problems, *Intl J. Num. Mether. Fluids* **24**, 1185–1210.

Freitas, C. J. & Street, R. L. 1988 Non-linear transport phenomena in a complex recirculating flow: a numerical investigation. *Intl J. Numer. Mether. Fluids* **8**, 769–802.

Freitas, C. J., Street, R. L., Findikakis, A. N. & Koseff, J. R. 1985 Numerical simulation of three-dimensional flow in a cavity. *Intl J. Numer. Mether. Fluids* **5**, 561–575.

Ghia, U., Ghia, K. N. & Shin, C. T. 1982 High-Re solutions of incompressible Navier–Stokes equations by coupled strongly implicit multigrid method. *J. Comput. Phys.* **48**, 387–411.

Guermond, J.-L. 1999 Un résultat de convergence à l'ordre deux en temps pour l'approximation des équations de Navier–Stokes par une technique de projection, *Modél. Math. Anal. Numér.* (M^2AN) **33**, 169–189.

Guermond, J.-L. & Quartapelle, L. 1997 Calculation of incompressible viscous flows by an unconditionally stable projection FEM. *J. Comput. Phys.* **132**, 12–33.

Guermond, J.-L. & Quartapelle, L. 1998 On the approximation of the unsteady Navier–Stokes equations by finite element projection methods. *Numer. Maths* **80**, 207–238.

Gustafson, K. & Halasi, K. 1986 Vortex dynamics of cavity flows. *J. Comput. Phys.* **64**, 279–319.

Kawaguti, M. 1961 Numerical solution of the Navier–Stokes equations for the flow in a two dimensional cavity. *J. Phys. Soc. Japan* **16**, 2307–2315.

Koseff, J. R. & Street, R. L. 1982 Visualization studies of a shear driven three-dimensionnal recirculating flow. *AIAA/ASME Thermophysics and Heat Transfer Conference, St Louis*, pp. 23–31.

Koseff, J. R. & Street, R. L. 1984*a* Visualization studies of a shear driven three-dimensionnal recirculating flow. *Trans. ASME: J. Fluids Engng* **106**, 21–29.

Koseff, J. R. & Street, R. L. 1984*b* On end wall effects in a lid-driven cavity flow. *Trans. ASME: J. Fluids Engng* **106**, 385–389.

Koseff, J. R. & Street, R. L. 1984*c* The lid-driven cavity flow: a synthesis of qualitative and quantitative observations. *Trans. ASME: J. Fluids Engng* **106**, 390–398.

Migeon, C. 2000 Contribution à l'analyse de l'écoulement tridimensionnel s'établissant à l'interieur de cavités cylindriques. Thèse de l'Université de Poitiers.

MIGEON, C., TEXIER, A. & PINEAU, G. 1998 Start-up flow in various trapezoidal-section lid-driven cavities. *ASME Fluids Engineering Division Summer Meeting*, June 21–25 Washington, DC.

MIGEON, C., TEXIER, A. & PINEAU, G. 2000 Effects of lid-driven cavity shape on the flow establishment phase. *J. Fluid Struct.* **14**, 469–488.

MILLS, R. D. 1965 On the close motion of a fluid in a square cavity. *J. R. Aero. Soc.* **69**, 116–120.

PAN, F. & ACRIVOS, A. 1967 Steady flows in rectangular cavities. *J. Fluid Mech.* **28**, 643–655.

PRASAD, A. K. & KOSEFF, J. R. 1989 Reynolds number and end-wall effects on lid-driven cavity flow. *Phys. Fluids A* **1**, 208–218.

RHEE, H., KOSEFF, J. R. & STREET, R. L. 1984 Flow visualization of a recirculating flow by rheoscopic liquid and liquid crystal techniques. *Exps. Fluids* **2**, 57–64.

SCHREIBER, R. & KELLER, H. B. 1983 Driven cavity flows by effective numerical techniques. *J. Comput. Phys.* **49**, 310–321.

SHANKAR, P. N. & DESHPANDE, M. D. 2000 Fluid mechanics in the driven cavity. *Annu. Rev. Fluid Mech.* **32**, 93–136.

TEMAM, R. 1969 Sur l'approximation de la solution des équations de Navier–Stokes par la méthode de pas fractionnaires. *Arch. Rat. Mech. Anal.* **33**, 377–385.

TEMAM, R. 1977 *Navier–Stokes Equations.* Studies in Mathematics and its Applications, vol. 2. North-Holland.

DE VAHL DAVIS, G. & MALLISON, G. D. 1976 An evaluation of upwind and central difference approximations by a study of recirculating flow. *Computers Fluids* **4**, 29–43.